Check for updates

JGR Solid Earth

RESEARCH ARTICLE
10.1029/2022JB025886

Dynamic Rupture Models, Fault Interaction and Ground Motion Simulations for the Segmented Húsavík-Flatey Fault Zone, Northern Iceland

Bo Li[1,2], Alice-Agnes Gabriel[1,3], Thomas Ulrich[1], Claudia Abril[4,5], and Benedikt Halldorsson[4,6]

[1]Department of Earth and Environmental Sciences, Ludwig-Maximilians-University, Munich, Germany, [2]Physical Science and Engineering Division, King Abdullah University of Science and Technology, Thuwal, Saudi Arabia, [3]Scripps Institution of Oceanography, UC San Diego, La Jolla, CA, USA, [4]Service and Research Division, Icelandic Meteorological Office, Reykjavík, Iceland, [5]Department of Earth Sciences, Uppsala University, Uppsala, Sweden, [6]Faculty of Civil and Environmental Engineering, School of Engineering and Natural Sciences, University of Iceland, Reykjavík, Iceland

Key Points:

- Observational constrained dynamic rupture scenarios of the Húsavík-Flatey Fault Zone match expected regional earthquake scaling and magnitudes
- Segmented fault geometry, hypocenter location, fault prestress and roughness affect rupture dynamics and ground motions
- Our physics-based scenarios show magnitude-consistent average attenuation relationships and match empirical ground motion models

Supporting Information:

Supporting Information may be found in the online version of this article.

Correspondence to:

B. Li,
bo.li.3@kaust.edu.sa

Citation:

Li, B., Gabriel, A.-A., Ulrich, T., Abril, C., & Halldorsson, B. (2023). Dynamic rupture models, fault interaction and ground motion simulations for the segmented Húsavík-Flatey Fault Zone, Northern Iceland. *Journal of Geophysical Research: Solid Earth*, *128*, e2022JB025886. https://doi.org/10.1029/2022JB025886

Received 22 OCT 2022
Accepted 16 MAY 2023

Author Contributions:

Conceptualization: Bo Li, Alice-Agnes Gabriel, Thomas Ulrich, Benedikt Halldorsson
Data curation: Bo Li, Alice-Agnes Gabriel, Thomas Ulrich, Benedikt Halldorsson
Formal analysis: Bo Li, Alice-Agnes Gabriel, Claudia Abril, Benedikt Halldorsson

© 2023 The Authors.
This is an open access article under the terms of the Creative Commons Attribution-NonCommercial License, which permits use, distribution and reproduction in any medium, provided the original work is properly cited and is not used for commercial purposes.

Abstract The Húsavík-Flatey Fault Zone (HFFZ) is the largest strike-slip fault in Iceland and poses a high seismic risk to coastal communities. To investigate physics-based constraints on earthquake hazards, we construct three fault system models of varying geometric complexity and model 79 3-D multi-fault dynamic rupture scenarios in the HFFZ. By assuming a simple regional prestress and varying hypocenter locations, we analyze the rupture dynamics, fault interactions, and the associated ground motions up to 2.5 Hz. All models account for regional seismotectonics, topo-bathymetry, 3-D subsurface velocity, viscoelastic attenuation, and off-fault plasticity, and we explore the effect of fault roughness. The rupture scenarios obey earthquake scaling relations and predict magnitudes comparable to those of historical events. We show how fault system geometry and segmentation, hypocenter location, and prestress can affect the potential for rupture cascading, leading to varying slip distributions across different portions of the fault system. Our earthquake scenarios yield spatially heterogeneous near-field ground motions modulated by geometric complexities, topography, and rupture directivity, particularly in the near-field. The average ground motion attenuation characteristics of dynamic rupture scenarios of comparable magnitudes and mean stress drop are independent of variations in source complexity, magnitude-consistent and in good agreement with the latest regional empirical ground motion models. However, physics-based ground motion variability changes considerably with fault-distance and increases for unilateral compared to bilateral ruptures. Systematic variations in physics-based near-fault ground motions provide important insights into the mechanics and potential earthquake hazard of large strike-slip fault systems, such as the HFFZ.

Plain Language Summary The Húsavík-Flatey Fault Zone (HFFZ) is the largest strike-slip fault in Iceland, located in the Tjörnes Fracture Zone in Northern Iceland where the largest earthquakes in Iceland have occurred. At present the seismogenic potential of HFFZ suggests that an earthquake of magnitude ~7 is possible, which poses a high earthquake hazard in the region. In this study, we generate a set of plausible earthquake rupture scenarios on the HFFZ that account for multi-physics, regional geology and topo-bathymetry. We simulate the corresponding seismic ground motions by exploring various assumptions, for example, in terms of slipping fault geometry and hypocenter locations. Our simulated scenarios have comparable magnitudes with historic events. The physics-based ground motion scaling conforms to new empirical ground motion models, but shows varying ground motion variability with distance. Our study provides an overview of multiple rupture scenarios on the HFFZ and suggests that an ensemble of physics-based dynamic rupture scenarios can complement classical seismic hazard assessment methods to better characterize the hazard in tectonically and seismically complex regions, especially in data-scarce regions.

1. Introduction

Iceland, the most seismically active region in Northern Europe, is located on the Mid-Atlantic Ridge, the divergent margin of the North American and Eurasian Plates. The Tjörnes Fracture Zone (TFZ) is located partially offshore in Northern Iceland and connects the on-land Northern Volcanic Zone with the offshore Mid-Atlantic Ridge. The TFZ consists of three sub-parallel fault systems (Einarsson, 1991): the Húsavík-Flatey fault zone (HFFZ), a ~100 km-long segmented right-lateral strike-slip fault system located at the center of the TFZ; the

21699356, 2023, 6, Downloaded from https://agupubs.onlinelibrary.wiley.com/doi/10.1029/2022JB025886 by Cochrane Germany, Wiley Online Library on [20/02/2024]. See the Terms and Conditions (https://onlinelibrary.wiley.com/terms-and-conditions) on Wiley Online Library for rules of use; OA articles are governed by the applicable Creative Commons License

Investigation: Bo Li, Alice-Agnes Gabriel, Thomas Ulrich, Benedikt Halldorsson
Methodology: Bo Li, Alice-Agnes Gabriel, Thomas Ulrich
Resources: Bo Li, Alice-Agnes Gabriel, Claudia Abril
Software: Bo Li, Thomas Ulrich
Supervision: Alice-Agnes Gabriel
Validation: Bo Li, Alice-Agnes Gabriel, Benedikt Halldorsson
Visualization: Bo Li, Alice-Agnes Gabriel, Thomas Ulrich
Writing – original draft: Bo Li, Alice-Agnes Gabriel, Thomas Ulrich
Writing – review & editing: Bo Li, Alice-Agnes Gabriel, Thomas Ulrich, Claudia Abril, Benedikt Halldorsson

Grímsey Fault Zone, an en-echelon fault system located ∼40 km NE of the HFFZ, with associated normal and strike-slip seismicity; and the Dalvík Fault Zone (DFZ), an enigmatic fault zone located south of the HFFZ (Figure 1a). The HFFZ is by far the largest transform fault in the TFZ and currently accommodates ∼1/4 of the total plate transform motion, estimated as 19.4 mm/year. The HFFZ fault segments align parallel to the direction of the regional tectonic deformation (Metzger & Jónsson, 2014).

The HFFZ poses a high earthquake hazard to the town of Húsavík and nearby coastal communities in Northern Iceland. Húsavík is located directly atop the eastern segment of the HFFZ and an important touristic site as the second largest town in the area. Several large historical earthquakes have been associated with the HFFZ. The most significant events are the 1755 M7.0 event and two M6.5 earthquakes in 1872 (Stefansson et al., 2008; Thorgeirsson, 2011). Metzger and Jónsson (2014) suggest that the seismic moment accumulated on the HFFZ since the last major earthquake in 1872 is equivalent to an earthquake of magnitude 6.8–7. The seismic source model of Snaebjornsson and Sigbjornsson (2007), designed for hazard assessment, divides the HFFZ into three planar segments from west to east, two NW-SE striking segments, and one NE-SW oblique segment. Their assumed maximum potential earthquake magnitudes on each segment, based on regression analysis of the frequency magnitude relationship of the earthquake catalog, are M_w7.3, M_w7.3, and M_w6.5, respectively.

In general, the seismic hazards in Northern Iceland are poorly constrained. Seismic studies in the area are challenged by the primarily offshore location of the TFZ, which includes large parts of the HFFZ. The Icelandic National Seismic Network (SIL) has recorded regional earthquakes since 1993, but the geometry of the TFZ and sparse distribution of SIL stations increase the uncertainty of earthquake locations and introduce biases (Hensch et al., 2013). Moreover, strong earthquakes did not occur in the TFZ during the operation of the SIL network, with the largest event being an M_w6 normal faulting event in 2020. Consequently, probabilistic seismic hazard assessment (PSHA) in Northern Iceland is challenging because the inherent limitation of the seismic catalog and instrumental recordings precludes placing firm observational constraints on seismic hazards. To address this issue and perform PSHA in Northern Iceland, previous studies (Solnes et al., 2004; D'Amico et al., 2016) used ground motion prediction equations (GMPEs) or ground motion models (GMMs) based on data sets from other seismic regions worldwide, or the Southern Iceland Seismic Zone (SISZ). SISZ is tectonically and seismically "symmetric" to the TFZ in Northern Iceland relative to the plate separation vector (Einarsson, 2008; Panzera et al., 2016), but denser instrumented.

The GMMs that were previously used for PSHA in Iceland and were calibrated to data from other seismic regions have been shown to be strongly biased against Icelandic strong motions (Kowsari et al., 2020). In addition, those developed using Icelandic data did not account for the saturation of amplitudes with increasing magnitudes (non-self-similar scaling) and/or near-fault magnitude-dependent distance scaling (Kowsari et al., 2020, 2021). While a new suite of empirical GMPEs has recently been developed that does not suffer from the above limitations (Kowsari et al., 2020), none of the empirical models specifically account for the complex near-fault effects associated with strong earthquake ruptures, particularly forward directivity effects. This motivates ground motion modeling using physics-based dynamic rupture models, constrained with locally and regionally seismic and geological data, to complement and constrain further the regional assessment of seismic hazard that the HFFZ poses in Northern Iceland, in particular to the town of Húsavík.

Previous studies have demonstrated the usefulness of deterministic earthquake models for improving ground motion predictions (e.g., Graves et al., 2011; Oral & Satriano, 2021; Rodgers et al., 2020). Although kinematic source descriptions do not guarantee physical consistency (P. M. Mai et al., 2016; Tinti et al., 2021), dynamic rupture simulations provide self-consistent models of how earthquakes start, propagate and stop and the associated seismic shaking (e.g., Gallovič et al., 2019; Guatteri et al., 2004; Schmedes et al., 2010). For example, Guatteri et al. (2003) showed that high degrees of heterogeneity and complexity of dynamic source models strongly affect near-fault ground motions. Dynamic rupture models can be used to better constrain kinematic source models for seismic ground motion modeling (e.g., Roten et al., 2012, 2014; Withers et al., 2019), and physics-based PSHA (Savran & Olsen, 2020). However, to model earthquake dynamics, choices regarding the required initial conditions, including the pre-existing state of stress and fault strength, as well as the fault geometries, are required (e.g., Ando & Kaneko, 2018; Tinti et al., 2021; Ulrich et al., 2022). Natural faults comprise both large-scale geometrical complexities (e.g., segmentation and branching), but also small-scale roughness (e.g., Ben-Zion & Sammis, 2003; Bistacchi et al., 2011; Candela et al., 2009; Power & Tullis, 1991; Sagy et al., 2007). Fault roughness results in small-scale complexities in the prestress distribution and poses additional resistance

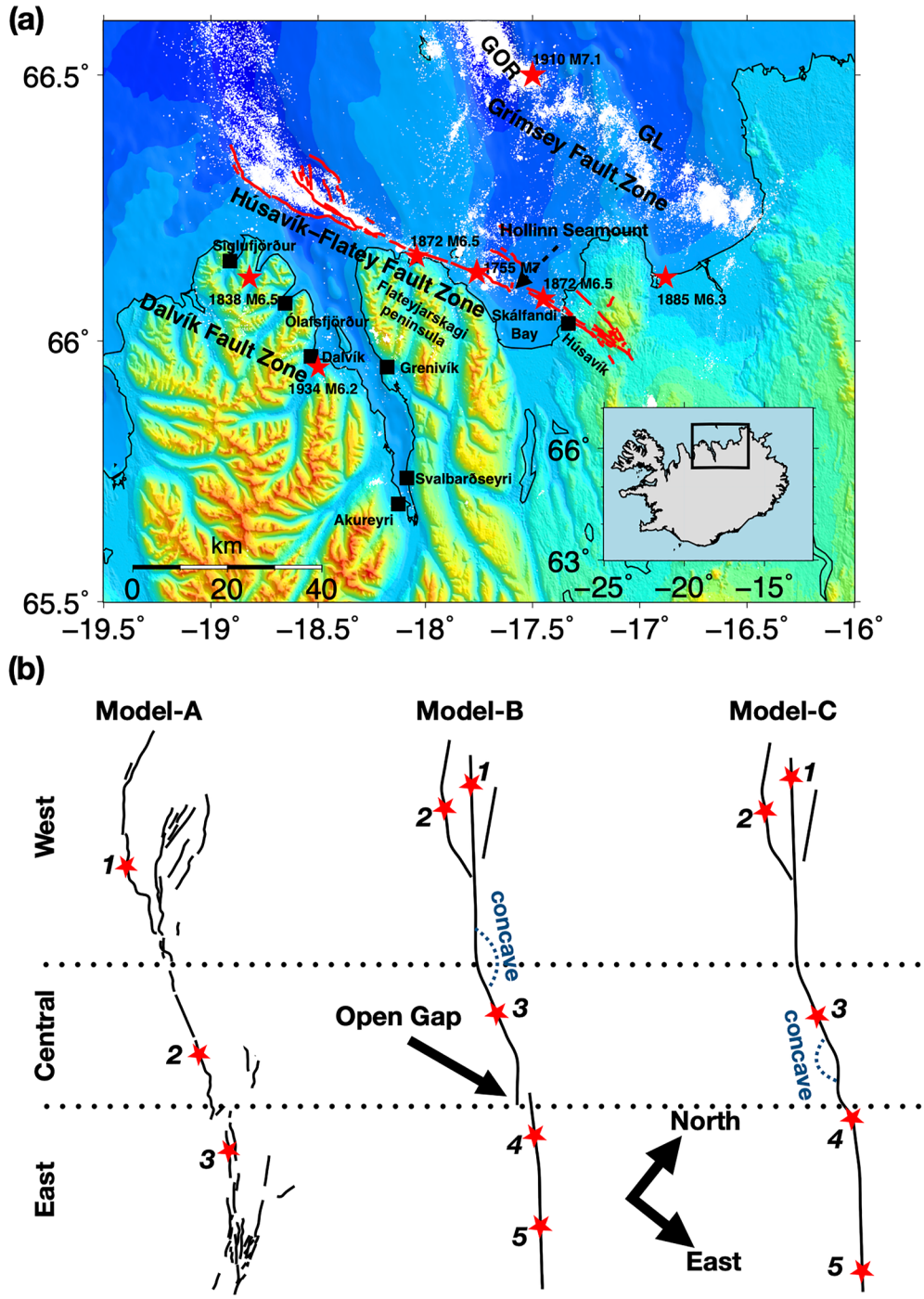

Figure 1. (a) Map of the coastal region of the Tjörnes Fracture Zone and its main towns (black squares) in relation to the complex segmented fault traces of the Húsavík-Flatey Fault Zone (HFFZ) (red lines) (Brandsdóttir et al., 2005; Halldórsson, 2019; Hjartardóttir et al., 2016; Magnúsdóttir et al., 2015). The clusters of white dots show relocated epicenters of earthquakes recorded from 1993 to 2019 (Abril et al., 2018, 2019), with red stars marking the approximate locations of large historical earthquakes (Stefansson et al., 2008; Thorgeirsson, 2011). The black dashed arrow points to the Hollinn Seamount which is located in the apparent gap of the HFFZ in Skjálfandi Bay. The inset shows a map of Iceland, with the black box indicating the zoomed-in study region. (b) HFFZ fault geometry models (shown here as rotated) used in dynamic rupture simulations with the black solid lines denoting the fault traces. Stars show the varied epicenter locations (hypocenters are at 7 km depth), with the index numbers identifying each rupture scenario. The two horizontal dotted lines divide the HFFZ into the western, central, and eastern sections. The complex Model-A is traced on the map. The blue dashed curves in Model-B and C mark the concave side of the fault geometry.

21699356, 2023, 6, Downloaded from https://agupubs.onlinelibrary.wiley.com/doi/10.1029/2022JB025886 by Cochrane Germany, Wiley Online Library on [20/02/2024]. See the Terms and Conditions (https://onlinelibrary.wiley.com/terms-and-conditions) on Wiley Online Library for rules of use; OA articles are governed by the applicable Creative Commons License

("roughness drag," Dunham et al. (2011)) to rupture. Fault roughness may affect the rupture dynamics, ground motion, and surface displacements (Bruhat et al., 2020; Dieterich & Smith, 2009; Fang & Dunham, 2013). Rough fault dynamic rupture simulations can generate broadband synthetic waveforms comparable to natural earthquakes (Shi & Day, 2013; Taufiqurrahman et al., 2022; Withers et al., 2019).

In this study, we develop a suite of 3-D spontaneous dynamic earthquake rupture scenarios on the HFFZ, based on varying levels of fault geometrical complexity, segmentation and hypocenter locations. We account for the regional 3-D subsurface structure, bathymetry and topography, viscoelastic attenuation, the possibility of nonlinear fault zone plasticity (off-fault yielding), and fault roughness. We investigate complex fault system interactions, in terms of co-seismic dynamic and static stress transfers and evaluate the potential for rupture cascading across the HFFZ. We systematically analyze the synthetic ground motions of comparable rupture scenarios and identify amplification patterns owing to rupture directivity, fault geometric complexity, and topography. We show that spontaneous dynamic rupture simulations can produce scenarios of comparable magnitudes to those of historic earthquakes and match empirical GMMs when informed by regional observations. Fully physics-based scenarios reveal more ground motion variability than that is typically captured in empirical approaches. The fault geometry, initial fault stress and strength are governed by dynamic trade-offs that are difficult to foresee without performing dynamic rupture simulations. The segmentation and complexity of fault geometry and differences in rupture dynamics, do not necessarily change distance-averaged ground shaking levels, but change the physically plausible maximum magnitude and near-field shaking levels.

2. Model Setup

2.1. Fault Geometries and Subsurface Model

The offshore location of most of the HFFZ and limited observational data pose challenges in estimating the fault geometry. Specifically, the connectivity between fault segments is poorly understood (see Section 5). In this study, we construct three fault models showing various levels of connectivity, from highly segmented to fully connected fault geometries, representing end-members of possible geometric complexity accounted for in seismic hazard assessment.

First, we construct a highly segmented model of the HFFZ (Figure 1b, Model-A), consisting of 55 partially intersecting, non-planar vertical faults, which also intersect with the complex bathy-topography of the free surface. This segmented model is based on (a) multibeam imaging and seismic reflection which have been used to map bathymetry in Northern Iceland (Brandsdóttir et al., 2005; Einarsson & Brandsdóttir, 2021; Magnúsdóttir et al., 2015); (b) the interpretation of two sets of relocated seismicity distributions (Figure 1a). The first set was estimated by using empirical travel times (Abril et al., 2018). The second data set was estimated by relocation using a three-dimensional tomographic model (Abril et al., 2021). The multibeam data has a resolution of approximately 10 m. However, fault trace complexity may not reflect the complexity of the fault morphology at depth; therefore, this resolution may not be representative of the effective uncertainty of the fault system geometry. We assume vertical faults that are supported by the depth distribution of the relocated seismicity considering the lateral variability of the crustal structure, with an average uncertainty less than 0.5 and 1 km in the horizontal and vertical directions, respectively (Abril et al., 2018, 2021).

We build a second fault system model, Model-B, which corresponds to a more simplified and less segmented geometry, acknowledging that the high complexity of mapped fault surface traces may not reflect the fault morphology at depth. This model is constructed by smoothing the small-scale geometrical complexities of Model-A, such as sharp kinks, and merging multiple, short segments. Model-B reduces the HFFZ to four fault segments, two main faults and two secondary faults in the west (Figure 1b, Model-B). The main fault segment spans the entire HFFZ and can be divided into three units: western, central and eastern sections. A ∼4 km-wide gap separates the central and eastern segments, which overlap over ∼1.5 km. This gap represents a prominent feature of the bathymetry in the middle of Skjálfandi Bay west of Húsavík, the Höllinn seamount (Figure 1a), which coincides with a sizable lateral offset in the HFFZ (Magnúsdóttir et al., 2015).

We design a third model, Model-C, which is based on Model-B but closes the gap between the central and eastern segments. This model reduces the complexity of Model-B to three segments (Figure 1b, Model-C). By comparing the results of dynamic rupture simulations using Model-B versus Model-C, we are able to investigate the role of the fault system gap for co-seismic fault interaction and ground shaking levels in the HFFZ.

21699356, 2023, 6, Downloaded from https://agupubs.onlinelibrary.wiley.com/doi/10.1029/2022JB025886 by Cochrane Germany, Wiley Online Library on [20/02/2024]. See the Terms and Conditions (https://onlinelibrary.wiley.com/terms-and-conditions) on Wiley Online Library for rules of use; OA articles are governed by the applicable Creative Commons License

21699356, 2023, 6, Downloaded from https://agupubs.onlinelibrary.wiley.com/doi/10.1029/2022JB025886 by Cochrane Germany, Wiley Online Library on [20/02/2024]. See the Terms and Conditions (https://onlinelibrary.wiley.com/terms-and-conditions) on Wiley Online Library for rules of use; OA articles are governed by the applicable Creative Commons License

In all dynamic rupture scenarios, we limit slip at depth by smoothly tapering deviatoric stresses from a depth of 9–11 km (see Section 2.2). This is motivated by the depth distribution of relocated seismicity, which is limited, on average, to a depth of 10 km (Abril et al., 2021). This depth range appears shallow compared to other regions (typically ~15 − 20 km) (e.g., Aderhold & Abercrombie, 2016), but is consistent with the warm lithosphere expected near a spreading center (e.g., Abercrombie & Ekström, 2001). We do not account for but discuss the effect of additional local variations in seismogenic depth (see Section 5). We embed all fault systems in a recent 3-D velocity model (Figure S1 in Supporting Information S1) that was also used for seismicity relocation (Abril et al., 2021) and use attenuation factors $Q_s = 50V_s$ (V_s in km/s) and $Q_p = 2Q_s$, following the empirical relations in Olsen et al. (2009).

2.2. Initial Stress and Fault Friction

We prestress the geometrically complex networks of non-planar vertical and partially intersecting faults of our HFFZ Models-A, -B, and -C with a laterally homogeneous regional stress field. We constrain a regional 3-D stress tensor from seismo-tectonic observations combined with physical assumptions on fault fluid pressurization and the Mohr-Coulomb theory of frictional failure, following Ulrich, Gabriel, et al. (2019). We also explore the effect of observational stress state uncertainties.

Our prestress and relative fault strength are fully defined using only four parameters:

1. The orientation of the regional maximum horizontal compressive stress $SH_{\max}$;
2. The stress shape ratio $s2_{\text{ratio}} = (s_2 - s_3)/(s_1 - s_3)$ with $s_1 > s_2 > s_3$ being the principal stress magnitudes. In our study, s_2 is vertical, and s_1 and s_3 are horizontal. s_1 points in $SH_{\max}$ direction and s_3 is normal to s_1;
3. The depth variation of the intermediate principal stress magnitude here assumed as a function of the confining stress times $1 - \gamma$. γ is the ratio of fluid pressure P_{fluid} to background lithostatic stress $\sigma_{zz} = \rho_{rock} gz$. $\gamma = \rho_{water}/\rho_{rock} = 0.37$ corresponds to a hydrostatic stress state assuming a 1-D rock density of 2,670 kg/m^3 and higher $\gamma > 0.37$ correspond to fluid overpressurized stress states;
4. The maximum prestress ratio R_0. The relative prestress ratio R (related to the seismic S parameter (Das & Aki, 1977) as $R = 1/(1 + S)$) is the ratio of the fault stress drop to the breakdown strength drop, and can be expressed as $(\tau - \mu_d \sigma_n')/((\mu_s - \mu_d)\sigma_n')$, in which τ is the shear stress on the fault, μ_s and μ_d are the static and dynamic friction coefficients, respectively, and σ_n' is the effective confining stress. The fault orientation relative to the orientation of the constant regional $SH_{\max}$ results in fault geometry-modulated variations in the relative prestress ratio R. We can constrain the smallest and largest principal stress components by prescribing R_0 which is the prestress relative to the strength drop on a virtual optimally oriented fault segment (Ulrich, Gabriel, et al., 2019). The regional optimal orientation is observationally constrained from inferences of $SH_{\max}$ and the stress shape ratio $s2_{\text{ratio}}$. In the static sense, an optimally oriented fault segment is one that, assuming homogeneous initial stress, strength, and homogeneous stressing rates, would reach failure before any other fault with different orientations. In dynamic rupture simulations, only a small portion of the fault must fail to nucleate a rupture (Ulrich, Gabriel, et al., 2019). $R_0 = 1$ indicating a critical prestress level on all optimally oriented faults (Aochi & Madariaga, 2003).

We follow Ziegler et al. (2016), who infer $SH_{\max} = 155 \pm 22°$ clockwise from the north and $s2_{\text{ratio}}$ ~0.5, from borehole breakouts, drilling-induced fractures, earthquake focal mechanism inversions, geological information and overcoring measurements. This is consistent with a previous study by Angelier et al. (2004), who inferred the orientation of the minor principal stress s_3 to be 65° and $SH_{\max} = 155°$ clockwise from the north, which is ~50° deviation with respect to the 105° azimuth plate transform motion. We assume an Andersonian stress state, with s_2 vertical, which is supported by the inference of a nearly vertical intermediate principal stress by Ziegler et al. (2016) and is consistent with the overall transform plate motion. We use the 1-D density model in Darbyshire et al. (2000) to calculate the depth-dependent confining stress, while the 3-D velocity structure of Abril et al. (2021) governs seismic wave propagation.

Frictional yielding and dynamic slip across all faults are constrained by a linear slip-weakening friction law (Andrews, 1976; Ida, 1972). The assumed static ($\mu_s = 0.55$) and dynamic ($\mu_d = 0.1$) friction coefficients are consistent with laboratory-derived values for a large variety of lithologies (e.g., Byerlee, 1978; Di Toro et al., 2011).

2.3. Model Parameterization

We systematically parameterize our dynamic rupture scenarios under varying geometries. Our main purpose is to generate comparable dynamic rupture scenarios in terms of magnitude and stress drop. We find that we need

21699356, 2023, 6, Downloaded from https://agupubs.onlinelibrary.wiley.com/doi/10.1029/2022JB025886 by Cochrane Germany, Wiley Online Library on [20/02/2024]. See the Terms and Conditions (https://onlinelibrary.wiley.com/terms-and-conditions) on Wiley Online Library for rules of use; OA articles are governed by the applicable Creative Commons License

Table 1
Dynamic Rupture Parameters for Model-A (Section 3.1) and Model-B (Section 3.2.1) and Model-C (Sections 3.2.2 and 3.3)

Parameter	Model-A	Models-B & -C
Static friction coefficient (μ_s)	0.55	0.55
Dynamic friction coefficient (μ_d)	0.1	0.1
Critical slip distance (D_c) within nucleation area (m)	**0.4**	**0.2**
Critical slip distance (D_c) outside nucleation area (m)	**0.4**	**0.5**
SH_{max}	155	155
Seismogenic depth (km)	10	10
Maximum prestress ratio (R_0)	**0.85**	**0.55**
Pore fluid ratio (γ)	**0.75**	**0.6**
Stress shape ratio ($s2_{ratio}$)	0.5	0.5
Nucleation radius (km)	1	1.5

Note. Fault network geometry specific differences are highlighted in bold.

to use different model parameters for complex geometry Model-A. We find these parameters in a sequence of several trial-and-error dynamic rupture simulations guided by the following priorities and trade-offs (all corresponding dynamic model parameters presented in Sections 3.1–3.3 are summarized in Table 1):

1. **Comparable magnitude.** Adding fault geometric complexity in the form of large-scale segmentation or fault roughness while leaving all other dynamic parameters constant leads to easier rupture arrest, less likely rupture jumping, or un-sustained ("dying") dynamic rupture reflecting in smaller magnitudes. For Model-A, we considerably increase R_0 which is a simple measure to balance the effects of geometric fault complexity.
2. **Comparable stress drop.** The trade-offs of the dynamic parameters of stress drop, strength drop, and fluid pressure ratio can be estimated as follows: $d\tau \sim R_0 g(0)(u_s - u_d)(1 - \gamma)\sigma_c$ (Equation 18 in Ulrich, Gabriel, et al. (2019)), where $d\tau$ is the stress drop, σ_c is the confining normal stress, and $g(0)$ is the stress concentration intensity, which is a constant value of 1 in our simulations. An excessively high stress drop leads to an unrealistically large slip, whereas a too low value leads to rupture arrest. Here, we increase the pore fluid pressure ratio γ for Model-A to achieve comparable stress drops with an increased R_0.
3. **Minimal critical nucleation.** Changing R_0 and γ changes the minimal-sized critical perturbation area which is sufficient to initiate self-sustained rupture. Thus, in Model-A a smaller nucleation size of 1 km is sufficient and we decrease D_c inside of the nucleation area to the same value as used outside the nucleation area for simplicity. In Model-B and -C, choosing a smaller D_c inside the nucleation can effectively reduce the otherwise larger, and less-comparable, required minimal nucleation size. We note that choosing a smaller D_c also enhances rupture cascading since a smaller area of a receiver fault needs to dynamically reach failure for rupture to jump.

Our models also account for the possibility of off-fault plasticity, and rupture nucleation is achieved by locally gradually reducing the fault strength, μ_s (Harris et al., 2018) (see Text S1 in Supporting Information S1). We ensure that the created meshes can accurately resolve seismic ground motions for proper resolution of 1 Hz by adapting SeisSol's mesh resolution to the 3-D velocity model (Breuer & Heinecke, 2022), with a higher resolved frequency (up to 2.5 Hz) in the vicinity of the fault system (Figure S2 in Supporting Information S1). More details can be found in Supporting Information S1. Here, we choose to resolve seismic waves up to 1 Hz everywhere in the model domain of interest, which balances computational cost with the resolution of the available observational datasets. If needed, a higher frequency resolution can be achieved by either decreasing the element size or using higher-order polynomial basis functions in SeisSol (e.g., Käser et al., 2008; Wollherr et al., 2018). Both will significantly increase time-to-solution. For example, halving the minimum shear wave velocity (or, doubling the highest frequency i.e., resolved) in one simulation requires approximately $2^4 = 16$ times the computation time on a regular mesh reflecting the three dimensions in space and the time dimension (Breuer & Heinecke, 2022). Note that SeisSol uses spatially adaptive unstructured meshes, which can be more efficient than simple estimates capture.

In Text S2 in Supporting Information S1, we explore the sensitivity of rupture dynamics to dynamic model parameter choices using Model-C geometry. We vary SH_{max} between 135° and 170° clockwise from the north, the $s2_{ratio}$ between 0.4 and 0.9, R_0 between 0.45 and 0.65, and the fluid pressure ratio γ between 0.55 and 0.70.

21699356, 2023, 6, Downloaded from https://agupubs.onlinelibrary.wiley.com/doi/10.1029/2022JB025886 by Cochrane Germany, Wiley Online Library on [20/02/2024]. See the Terms and Conditions (https://onlinelibrary.wiley.com/terms-and-conditions) on Wiley Online Library for rules of use; OA articles are governed by the applicable Creative Commons License

3. 3-D Dynamic Rupture Scenarios

We first investigate the effects of fault geometry on rupture dynamics across the three HFFZ models. For each fault geometry, we generate unique rupture scenarios (three for Model-A, five for Model-B, and five for Model-C) by varying the hypocenter locations (indicated by stars in Figure 1b). We present a smaller number of scenarios based on Model-A. We find only a few different multi-fault large-magnitude earthquake scenarios, with reasonable stress drop and slip, can be obtained with this highly segmented fault geometry and our model assumptions. Figure S3 in Supporting Information S1 shows that our Model-B and Model-C scenarios fit the finite-source inversion-derived scaling law of P. Mai and Beroza (2000) well for the effective rupture area (based on the autocorrelation of the slip function) and average slip. These scaling relationships have also been recently validated to best fit the source dimension estimates of South Iceland earthquakes (Bayat et al., 2022). However, our models overshoot the scaling of the rupture length, which directly reflects regional shallow locking depths. We omit a direct comparison with scaling laws for Model-A scenarios because of the high segmentation and coalescence of faults (Scholz et al., 1993). For this suite of 13 scenarios, we analyze the effect of fault geometry, rupture directivity, and topography on ground motion characteristics. We perform four additional scenarios by adding fault roughness.

3.1. Dynamic Rupture Scenarios for a Highly Segmented Húsavík-Flatey Fault Zone Geometry (Model-A)

We show three dynamic rupture scenarios across the most complex fault system (Model-A). We assume a hypocentral depth of 7 km and test varying epicenter positions within the western (scenario A1), central (scenario A2), and eastern (scenario A3) sections of the HFFZ. In trial-and-error simulations (not shown) varying hypocentral depth between 3, 5, and 7 km, we find that hypocenters at a depth of 7 km promote multi-fault rupture, and allow generating scenarios with magnitudes similar to historic events. We choose hypocentral locations based on the inferred epicenters of significant historical earthquakes such as the 1755 magnitude 7 (scenario A2) and 1872 magnitude 6.5 (scenario A3) events (Stefansson et al., 2008; Thorgeirsson, 2011). There are no large historic events associated with the epicenters in the western part of the HFFZ (scenario A1). Uncertainties in the magnitude estimates of historical earthquakes (Thorgeirsson, 2011) have not been systematically evaluated and may be significant. The spontaneously evolving dynamic rupture scenarios A2 and A3 with moment magnitudes M_w6.91 and M_w6.50, respectively, have comparable magnitudes to these historic earthquakes, which is an important result given that we do not prescribe rupture propagation and arrest.

All three scenarios exhibit complex rupture sequences. Rupture cascading across multiple fault segments leads to rupture-front segmentation into multiple rupture fronts. 3-D subsurface impedance contrasts and free surface interactions cause additional rupture complexity, such as healing due to reflected and interface waves (e.g., Dunham, 2005; Huang & Ampuero, 2011) and back-propagating rupture fronts (e.g., Beroza & Spudich, 1988; Fliss et al., 2005). To illustrate the complexity of Model-A ruptures, we show in Figure 2 the key characteristics of the A2 scenario that is associated with the dynamic rupture of 13 fault segments of the complex fault system (Figure 2a). The rupture scenario features multiple dynamic triggering episodes (Figure 2b and Movie S1) with irregular temporal progression in the seismic moment release rate (Figure 2c).

The A2 scenario features localized supershear episodes, and dynamic complexity such as delayed or remote dynamic triggering and backward-propagating rupture fronts (Figure 2b). Dynamic earthquake rupture takes first the form of a bilateral symmetrically propagating crack propagating away from the hypocenter at a sub-shear/sub-Rayleigh rupture speed on fault segment 24 (F24). The rupture reaches the western edge of F24 at a simulation time of 1 s, and 2 s later reaches the eastern edge. The rupture of F55 to the west is dynamically triggered, at 6–7 km depth, at approximately 3 s simulation time, and rapidly gains momentum on this more optimally oriented segment. A supershear daughter crack forms ahead of the main crack. Next, F14, F17, and F16 are triggered to the west and are fully ruptured at 7 s simulation time. After a 3 s long delay, associated with the first obvious trough in the seismic moment release rate, segment F26 to the east of the nucleation region is dynamically triggered and fully ruptured. During this period, the parallel fault segment F25 does not break. The rupture continues further east, with dynamic triggering of the next segment (F30). Meanwhile, the rupture on F25 starts to nucleate but dies out quickly. After a short delay, the rupture jumps across a step-over and initiates on segment F33 at a depth of ∼8 km. It then ruptures bilaterally across the entire segment F33 at 13 s simulation time. This results in rupture expanding updip and backward, to the west. Then, the rupture on F25 to the west re-nucleates

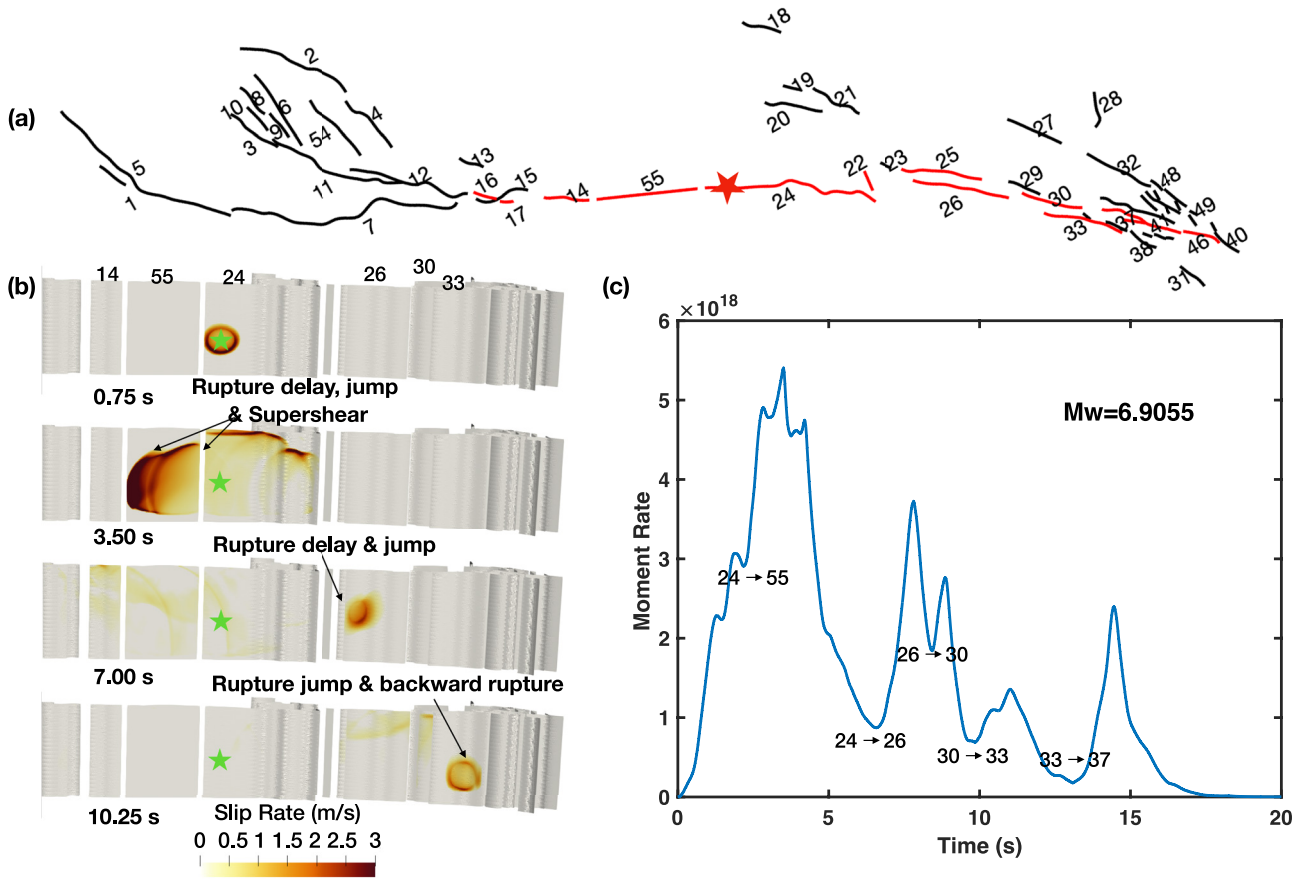

Figure 2. Dynamic rupture scenario A2 across the highly segmented Model-A fault network. (a) Map view of the fault traces for Model-A, with numbers denoting the fault segment index. The red lines mark the fault segments that ruptured in scenario A2. Some small segments in the east are not indexed. The red star indicates the epicenter location. (b) Snapshots of the absolute slip rate, highlighting the complex rupture process at rupture times of 0.75, 3.50, 7.00, and 10.25 s. The labels indicate noteworthy features of the rupture. Fault segments in the west of the Húsavík-Flatey Fault Zone that did not rupture in A2 are not shown. The green star indicates the hypocenter location. (c) The time evolution of the modeled multi-peak seismic moment release rate, with the index pairs indicating dynamic triggering (rupture jumping) across fault segments that correlate with moment rate troughs.

again and breaks about 4/5 of that segment. To the east, the rupture jumps through another step over, triggers rupture at the conjunction of F41 and F37, ruptures bilaterally, and finally breaks the entire segments of F37, F41, and F46 to the east. This is associated with the final peak of the moment rate function at ~14 s. Scenario A2 results in the rupture of 13 segments over 17 s with a moment magnitude of $M_w = 6.91$.

The three scenarios A1, A2, and A3 all involve different rupture sequences and segments and yield different slip distributions (Figure 3a). The segments that spontaneously slip in scenario A3 also rupture in scenario A2. Generally, more slip accumulated centrally on each ruptured segment. The maximum slip reaches ~2.8, 4.2, and 2.5 m for the three scenarios. Our models produce variable shallow slip, with nearly no shallow slip deficit (SSD) at certain locations, for example, on segment F55, west of the nucleating fault (F24) in scenario A2 (Figure S4 in Supporting Information S1). Such a distinct lack of SSD has been reported for submerged supershear rupture (Socquet et al., 2019), and mature fault zones (Dolan & Haravitch, 2014) and has important implications for seismic hazards and the long-term seismic cycle. The high slip across the entire seismogenic width of segment F55 in scenario A2 is potentially promoted by local supershear rupture (Hu et al., 2016) (Figure S5 in Supporting Information S1).

Maps of the resulting ground motions (SA [1.0 s]) are shown in Figure 3 for all three rupture scenarios of the complex fault network Model-A. Spectral acceleration is calculated from RotD50 (SA [1.0 s]), the 50 percentile spectral acceleration of period 1 s of the set of geometric means obtained using all non-redundant rotations between 0 and 90° (Boore et al., 2006). Rotation-invariant measures are commonly used in GMMs and are

21699356, 2023, 6, Downloaded from https://agupubs.onlinelibrary.wiley.com/doi/10.1029/2022JB025886 by Cochrane Germany, Wiley Online Library on [20/02/2024]. See the Terms and Conditions (https://onlinelibrary.wiley.com/terms-and-conditions) on Wiley Online Library for rules of use; OA articles are governed by the applicable Creative Commons License

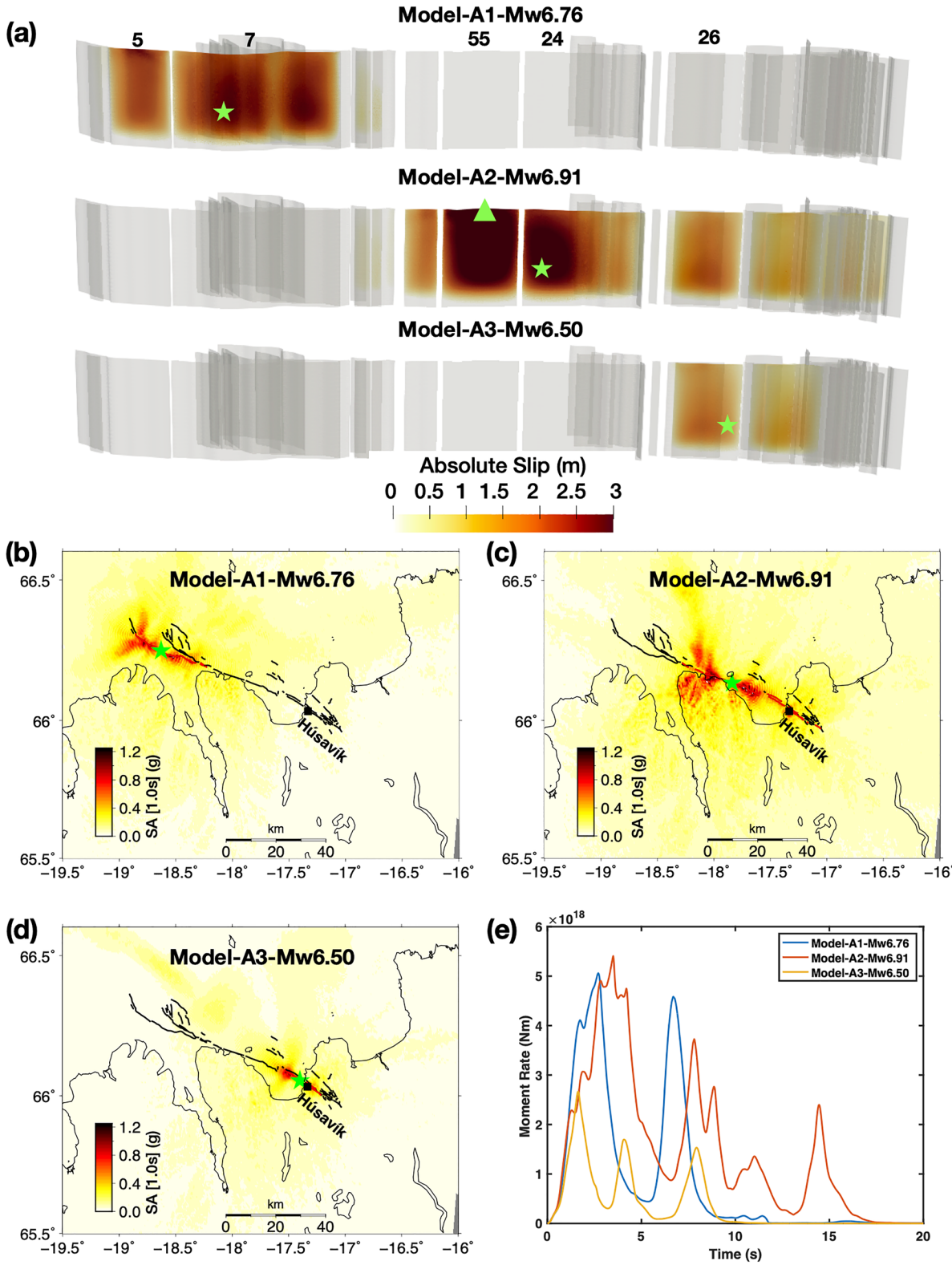

Figure 3. Accumulated fault slip distribution and ground motion (spectral acceleration SA[1.0 s] in g) for three rupture scenarios using Model-A with varying hypocenter locations. (a) Each scenario features distinct dynamics and involves different fault segments. The moment magnitudes of scenarios A2 (M_w6.91) and A3 (M_w6.50) resemble historical events with similar epicenters. The green triangle mark the location showing the shallow slip deficit in Figure S4 in Supporting Information S1. (b–d) Ground motion maps ([SA 1.0s] in g). (e) Moment rate functions.

21699356, 2023, 6, Downloaded from https://agupubs.onlinelibrary.wiley.com/doi/10.1029/2022JB025886 by Cochrane Germany, Wiley Online Library on [20/02/2024]. See the Terms and Conditions (https://onlinelibrary.wiley.com/terms-and-conditions) on Wiley Online Library for rules of use; OA articles are governed by the applicable Creative Commons License

21699356, 2023, 6, Downloaded from https://agupubs.onlinelibrary.wiley.com/doi/10.1029/2022JB025886 by Cochrane Germany, Wiley Online Library on [20/02/2024]. See the Terms and Conditions (https://onlinelibrary.wiley.com/terms-and-conditions) on Wiley Online Library for rules of use; OA articles are governed by the applicable Creative Commons License

calculated to conform to those used by regional empirical GMMs (Kowsari et al., 2020). However, for the purpose of analyzing directivity effects in the near-fault region, the horizontal component rotated along the strike-normal direction should be inspected separately (Spudich et al., 2014). We find heterogeneous ground shaking intensities across and along the fault system. Higher-intensity shaking is localized in the vicinity of fault geometrical complexities, such as fault bends or gaps between segments, in the direction of rupture propagation. We isolate this geometric effect in the Model-B and Model-C scenarios (see Section 3.2). We relate this to rapid rupture acceleration and deceleration due to geometrically modulated locally different prestress conditions, as well as barrier effects (e.g., Oglesby & Mai, 2012).

3.2. Dynamic Rupture Scenarios for Simplified Húsavík-Flatey Fault Zone Geometries (Model-B and Model-C)

To compare with the scenarios using the highly complex 55-segment fault network of Model-A, we carry out dynamic rupture scenarios on more simplified and smooth fault geometries to investigate the effects of fault geometry and segmentation on rupture dynamics and the resulting ground motion characteristics. We pay special attention to the location of the Hóllinn seamount (Figure 1a), which coincides with a sizable lateral gap in the geometry of the HFFZ in Model-B. This gap may potentially arrest the propagating fault rupture on either side, thereby curbing the maximum earthquake magnitude potential of the HFFZ and the corresponding near-fault ground motion intensities.

3.2.1. "Open Gap" Between the Central and Eastern HFFZ (Model-B)

Multiple dynamic rupture scenarios are performed on the 4-segment geometry of Model-B, each of which with a different hypocentral location prescribed along the fault system. We refer to the epicenter indices in Figure 1b as scenario identifiers. We use the model parameters summarized in the last column of (Table 1). As detailed in Section 2.3, we use a slightly lower R_0, decreased γ, larger nucleation radius, and larger D_c to achieve rupture dynamics comparable to the more segmented Model-A geometry.

The simpler geometry of Model-B leads to dynamic rupture scenarios characterized by simpler rupture processes. The adapted dynamic rupture parameters render all faults in the Model-B and Model-C scenarios dynamically stronger (Ulrich, Gabriel, et al., 2019) and less critically loaded; thus, they are more resistant to slip. However, rupture arrest and thus slip are predominantly limited by the remaining complexities in the fault geometry. Importantly, none of the explored rupture scenarios could jump across the gap between the central and eastern segments. We note that the larger D_c and lower pore fluid pressure in Model-B and -C impede dynamic triggering but can produce scenarios with realistic slip, rupture speed, magnitudes, and scaling behavior.

Figure 4a and Movie S2 illustrate the simpler rupture process of scenario B3, representing an exemplary Model-B scenario. The rupture is nucleated at the center of the fault system and propagates bilaterally. The rupture to the east terminates when reaching the open gap at 7.2 s rupture time. This time coincides with the peak in the seismic moment release rate (Figure 4b). The westward rupture front breaks the entire central segment and branches to the western segment, which then ruptures integrally. This leads to a M_w7.15 event with a duration of 19 s. The earthquake rupture scenarios of Model-B, which break the same segments, have similar moment magnitudes, whereas their varying hypocenter locations modulate the accumulated fault slip distributions (Figure 5). For instance, scenarios B1 and B3 both rupture the western and central segments of the main fault and have the same moment magnitude (M_w7.15). However, the large slip asperity is shifted westward in scenario B3 compared to scenario B1. In scenarios B4 and B5, the position of the high-slip asperity depends on the hypocenter location.

Owing to the smoother geometry of Model-B, the synthetic shake maps exhibit less spatial heterogeneity than those of Model-A. In addition, the scenarios result in ground shaking intensities that show very strong and expansive directivity effects. These are promoted by long and smooth faults and appear for both bilateral (B2, B3, and B4) and unilateral ruptures (B1 and B5). Figure 6 shows the RotD50 measure of SA[1.0 s]. As expected, the highest ground-motion intensities are observed in the forward rupture direction. Notably, several of the scenarios present asymmetric ground motions with respect to faults. The amplified ground motions are located on the concave side of the slipping fault. For instance, scenarios B1 and B3 generate stronger ground motions on the northern side of the western segment of the main fault and on the southern side of the eastern part of the central segment. Similar to our segmented Model-A based dynamic rupture scenarios, rapid isochrone acceleration and deceleration due to the rupture velocity and direction change at geometric complexities (Figure S6 in Supporting

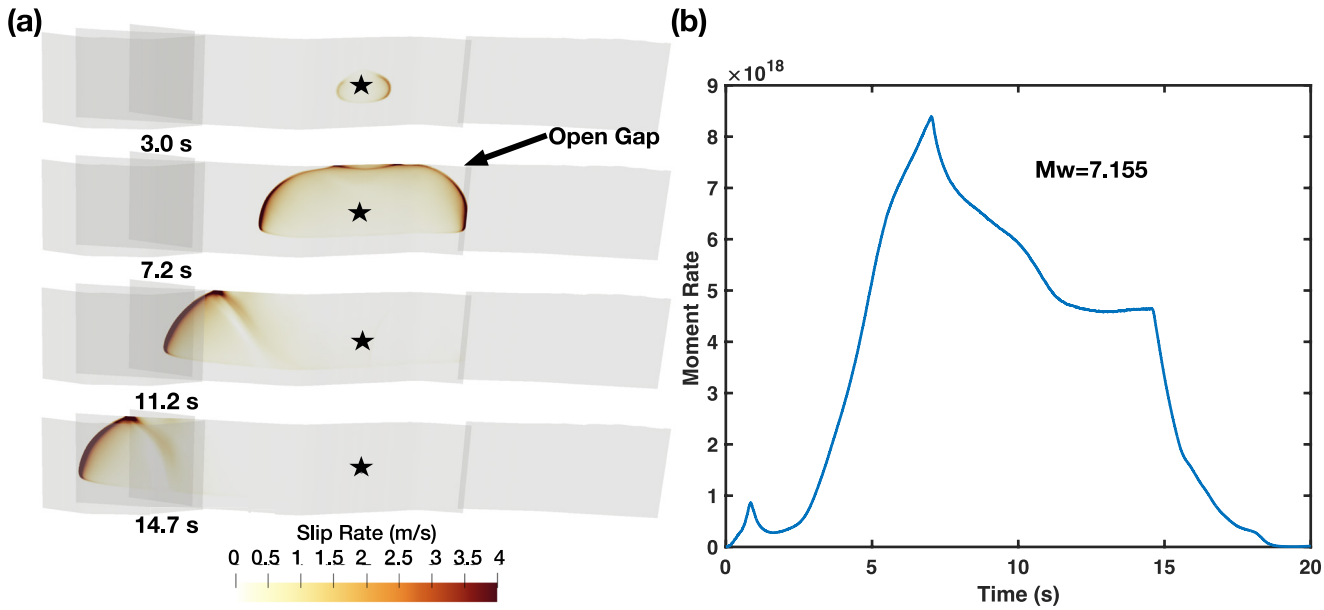

Figure 4. Overview of the simulated rupture propagation of scenario B3 using Model-B fault system geometry. (a) Snapshots of the absolute slip rate are shown at rupture times of 3.0, 7.2, 11.2, and 14.70 s. (b) Seismic moment release rate for scenario B3. The low-amplitude first peak of the moment rate function is due to changes in rupture speed during the forced nucleation and a sharp change from smaller Dc (0.2 m) within to larger Dc (0.5 m) outside the nucleation area.

Information S1) generate intense ground motions. These fault complexities, for example, fault bends, pose locally different prestress conditions for rupture propagation. Bands with larger ground motion amplitudes form at an acute angle with respect to the rupture direction. This results in asymmetric shaking around the smooth fault (see Figure 6). In addition, smaller-scale topography features imprint the ground motion maps, as illustrated in Figures 6a and 6f, especially the topographical features of the Flateyjarskagi Peninsula south of the central HFFZ. Such topographic effects on ground motion can be the consequence of the scattering of seismic waves

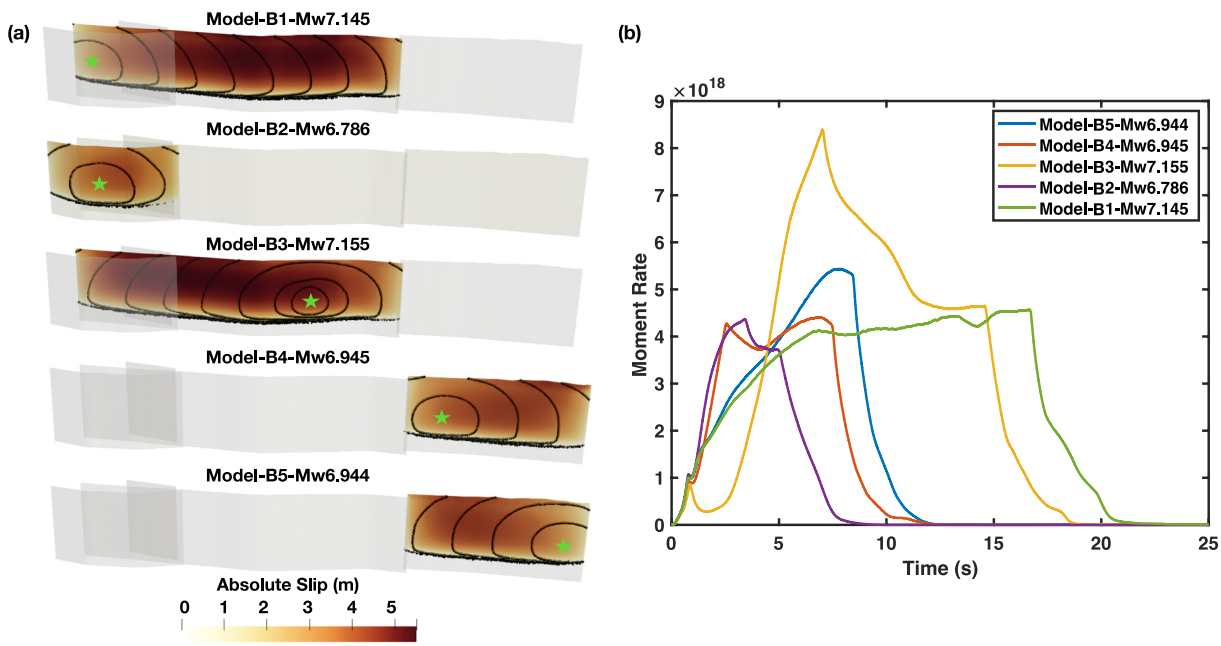

Figure 5. (a) Accumulated fault slip distribution of five rupture scenarios across Model-B, with different hypocenter locations. The green star marks the hypocenter location at a depth of 7 km in all the scenarios. The black contours are isochrones of the rupture time, with 2 s intervals. (b) Moment rate functions for the five rupture scenarios in (a). None of the explored scenarios are able to jump across the gap between the central and east segments.

21699356, 2023, 6, Downloaded from https://agupubs.onlinelibrary.wiley.com/doi/10.1029/2022JB025886 by Cochrane Germany, Wiley Online Library on [20/02/2024]. See the Terms and Conditions (https://onlinelibrary.wiley.com/terms-and-conditions) on Wiley Online Library for rules of use; OA articles are governed by the applicable Creative Commons License

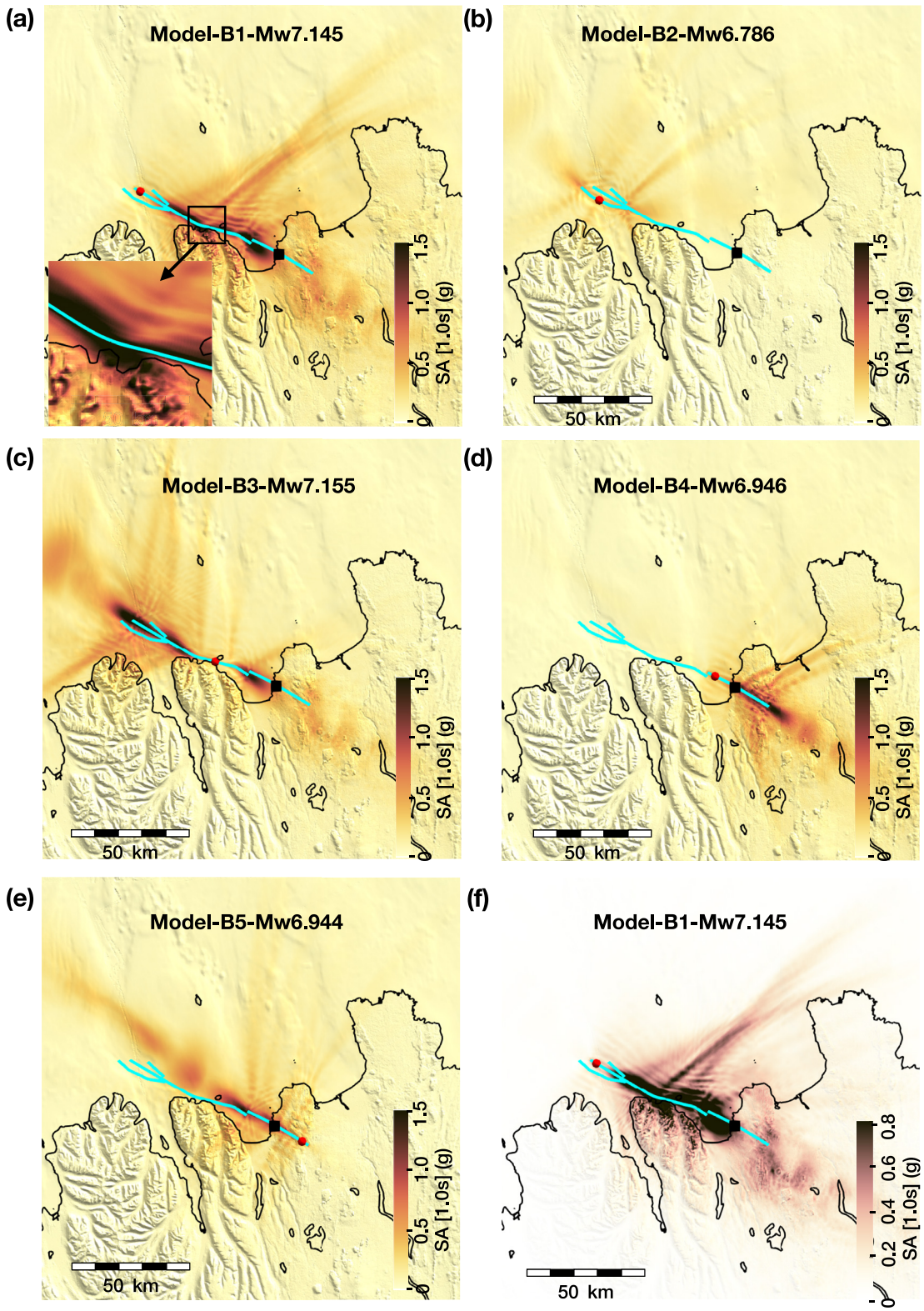

Figure 6. Ground motions (spectral acceleration SA[1.0 s] in g) for five rupture scenarios across Model-B, shown in panels (a)–(e). Here we show a zoomed-in view of the modeling domain around the fault traces to illustrate the ground motion characteristics in the local region. In addition, we zoomed in the black box region in (a) to demonstrate the geometric effects on ground motions. The cyan lines indicate the fault traces. The red circle marks the hypocenter location for each scenario. The black square show the location of Húsavík town. The color maps are saturated to better capture the spread of ground shaking away from the fault network. Panel (f) is the same as panel (a), but with a narrower range colormap and using an opacity filter to highlight smaller-scale amplification of topography features.

21699356, 2023, 6, Downloaded from https://agupubs.onlinelibrary.wiley.com/doi/10.1029/2022JB025886 by Cochrane Germany, Wiley Online Library on [20/02/2024]. See the Terms and Conditions (https://onlinelibrary.wiley.com/terms-and-conditions) on Wiley Online Library for rules of use; OA articles are governed by the applicable Creative Commons License

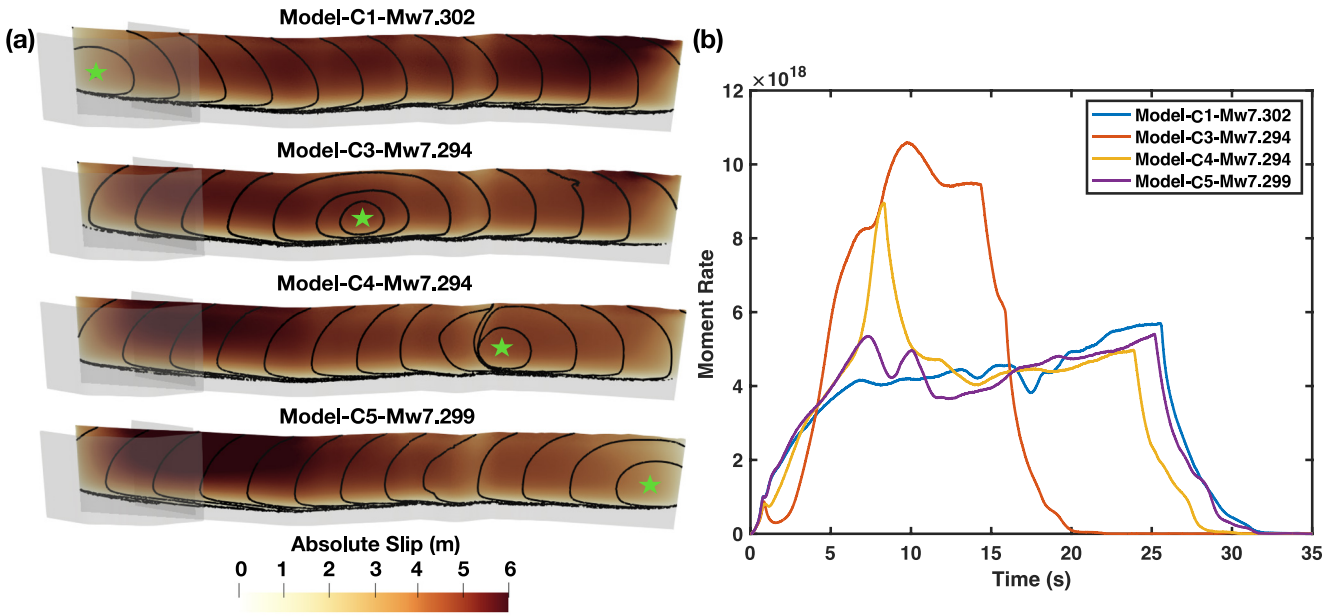

Figure 7. All Model-C scenarios rupture the entire main fault and do not activate other fault segments. (a) Accumulated fault-slip distribution for four rupture scenarios across Model-C. We omit scenario C2 because it is equivalent to scenario B2. Green stars indicate the hypocenter locations for each scenario. The black contours are the 2 s isochrones of the rupture time. (b) Moment rate functions for the four rupture scenarios in (a).

and the redistribution of energy (Ma et al., 2007; Taufiqurrahman et al., 2022). Our SA[1.0 s] maps show generally consistent characteristics (Bradley, 2012) with synthetic maps of Peak Ground Velocity (PGV, measured as RotD50), which is less sensitive to high frequencies (Figure S7 in Supporting Information S1). Future targeted simulations may resolve spectral acceleration at higher frequencies and for specific sites.

3.2.2. "Closed Gap" (Model-C)

Model-B scenarios demonstrate that a significant lateral offset between the eastern and central HFFZ can arrest dynamic earthquake rupture and thus reduce the maximum possible earthquake magnitude on the fault system. In this section we "close the gap" (Model-C) to investigate alternative and potentially worst-case earthquake scenarios with the potential of rupturing the whole HFF. This could also lead to large-amplitude ground motion, particularly in coastal areas. We define five dynamic rupture scenarios on the geometry of Model-C by varying the hypothetical hypocentral positions (Figure 1b). We use the same model parameters as for Model-B scenarios. Note that we show only 4 scenarios for Model-C because scenario C2 and B2 are identical.

In contrast to Model-B scenarios, all Model-C scenarios result in the rupture of the entire main fault and no activation of other fault branches. This leads to M_w7.3 moment magnitudes. The full connectivity of the main fault results in simple rupture dynamics in all scenarios, leading to relatively smooth and less varying fault slip distributions that are modulated by varying hypocenter locations (Figure 7a). As an example, we detail the rupture dynamics of Model-C3 in Figure S8 in Supporting Information S1 and Movie S3. Patches of large slip coincide with fault segments relatively far from the hypocenter. For example, in scenarios C1 and C3, peak slip occurs on the eastern segments, whereas it localizes on the western segment in scenarios C4 and C5. The smooth fault geometry and lack of small-scale structural heterogeneity in our models promote laterally mostly invariant and depth-dependent only rupture velocity, indicated by the regular intervals of the rupture time contours along the fault (Figure 7a). However, the incipient westward rupture in scenario C4 features a rupture delay of a few seconds coinciding with the change in fault geometry at the connection between the eastern and central segments, that is, where the gap has been closed. The insignificant variation in the rupture speed and slip distribution along-strike (in the rupture propagation direction) translates into trapezoid-shaped seismic moment rate release functions (Figure 7b). Their shapes are modulated by varying the hypocentral locations, which promote unilateral or bilateral ruptures. Bilateral ruptures are of shorter duration and, therefore, show a higher rate of moment release.

Maps of the ground motions are shown in Figure 8. To better illustrate the effects of rupture directivity and fault geometry, we show the ground motion intensity distribution along two cross-sections perpendicular to the

21699356, 2023, 6, Downloaded from https://agupubs.onlinelibrary.wiley.com/doi/10.1029/2022JB025886 by Cochrane Germany, Wiley Online Library on [20/02/2024]. See the Terms and Conditions (https://onlinelibrary.wiley.com/terms-and-conditions) on Wiley Online Library for rules of use; OA articles are governed by the applicable Creative Commons License

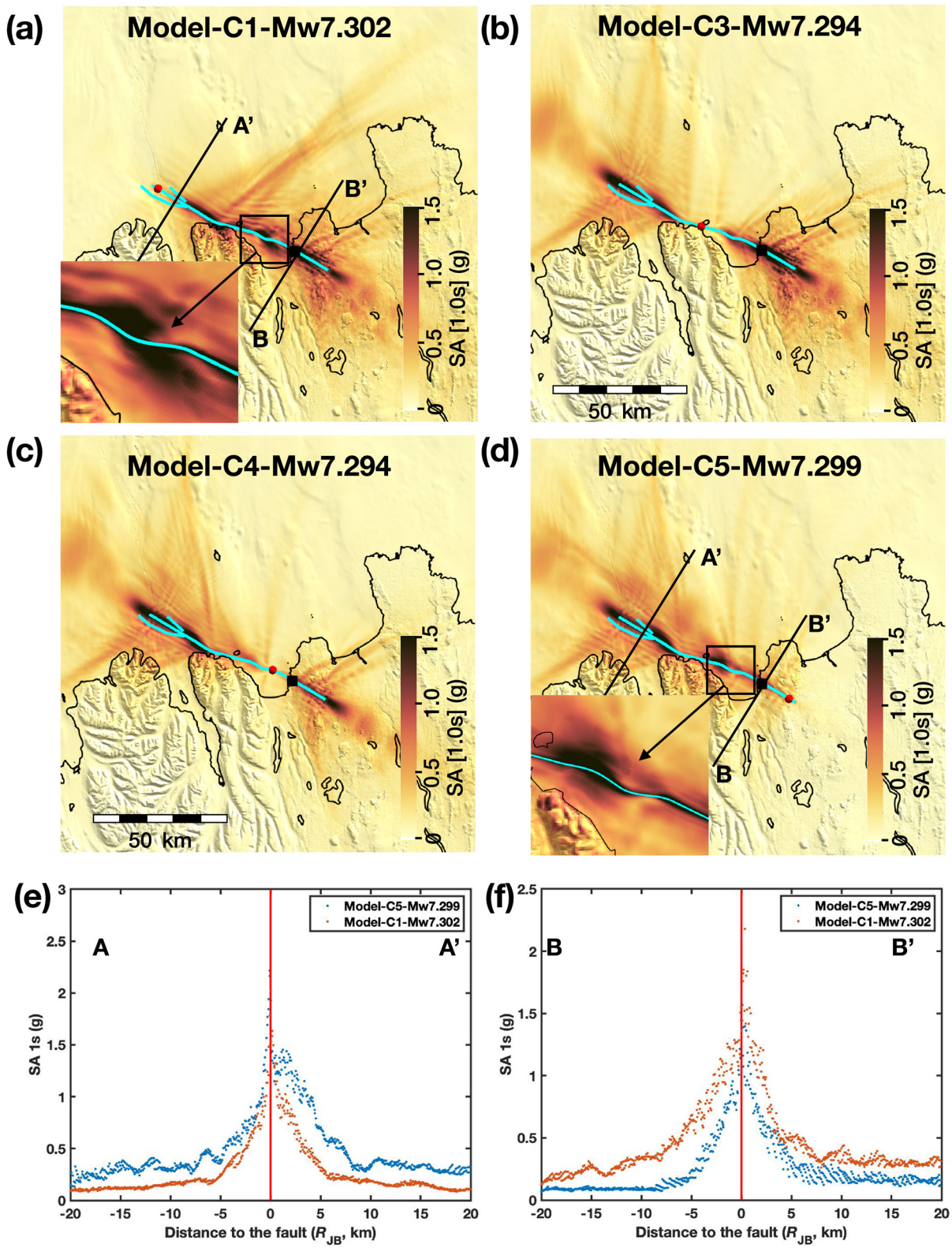

Figure 8. (a)–(d) Ground motions (spectral acceleration SA[1.0 s] in g) for four rupture scenarios across Model-C. We zoomed in the black box region in (a) and (d) to demonstrate the geometric effect on ground motions. The cyan lines show the fault traces. The red circle marks the hypocenter location for each scenario. The black square shows the location of the Húsavík town that sits on the eastern segment of the fault. Color maps are saturated to better capture the spread of ground motions. (e)–(f) Ground motions (SA[1.0 s]) along cross sections A–A' and B–B' for scenarios C1 and C5. The vertical red lines show the fault location.

21699356, 2023, 6, Downloaded from https://agupubs.onlinelibrary.wiley.com/doi/10.1029/2022JB025886 by Cochrane Germany, Wiley Online Library on [20/02/2024]. See the Terms and Conditions (https://onlinelibrary.wiley.com/terms-and-conditions) on Wiley Online Library for rules of use; OA articles are governed by the applicable Creative Commons License

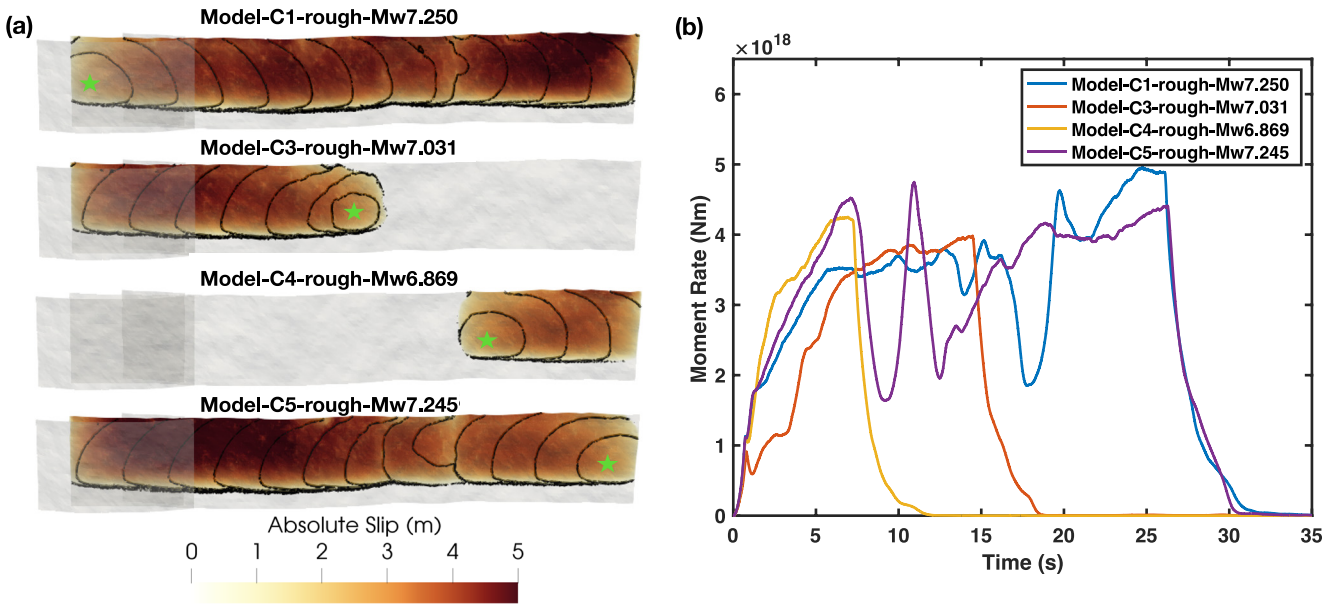

Figure 9. (a) Accumulated fault slip distribution of four Model-C scenarios incorporating fault roughness. Green stars indicate the hypocenter locations for each scenario. The black contours are 2 s isochrones of rupture time. (b) Moment rate functions for the four rupture scenarios in (a).

western (A–A') and eastern (B–B') segments, respectively for two scenarios, C1 and C5. The rupture directivity causes heterogeneous ground motion intensities. Ground motions are amplified in the forward-rupture direction, illustrated as higher ground shaking intensities along cross-section A-A' in scenario C5 than those in scenario C1, and inversely for cross-section B-B'. Depending on the scenario, both symmetric and asymmetric ground motion patterns are observed across linear fault segments. Ground motion asymmetry is caused by the coupled effects of rupture directivity and fault geometry. For example, the unilateral rupture from west to east in scenario C1 (red dots in Figure 8e) results in an overall symmetric pattern along A–A' across the straight fault segment in the west. In contrast, the rupture from east to west in scenario C5 breaks through the fault kink between the central and western segments before reaching the western linear fault segments. This results in an asymmetric pattern (blue dots in Figure 8e) along the same cross-section with generally higher ground motions on the northern side of the fault, especially at a near-fault distance of less than 5 km. The same coupled effect also leads to a symmetric pattern along B–B' across the eastern fault segments for scenario C5 and an asymmetric distribution for C1, depending on whether the rupture has broken through fault complexities before reaching the linear fault segments.

3.3. Fault Roughness

Here, we explore the effect of fault roughness based on Model-C. We construct and mesh rough, intersecting fault planes with a self-similar fractal distribution over length scales from 200 m to 50 km and assume an amplitude-to-wavelength ratio α equal to 10^{-2}. The amplitude-to-wavelength ratio of natural faults ranges from 10^{-4} to 10^{-2} (Power & Tullis, 1991). Our choice allows direct comparability with earlier studies (e.g., Bruhat et al., 2020; Fang & Dunham, 2013; Shi & Day, 2013; Taufiqurrahman et al., 2022).

The high-frequency radiation is enhanced in our rough fault dynamic rupture models without additional prestress heterogeneity. Adding fault roughness changes the rupture dynamics; however, it does not negatively impact the achieved consistency in terms of modeling realistic magnitudes. Our simulations, which incorporate fault roughness, leave all other dynamic parameters the same. To identify our four scenarios incorporating fault roughness, we append an "-R" to their names. Scenarios C1-R and C5-R have slightly lower magnitudes than scenarios C1 and C5, and their final fault slip distributions are more heterogeneous (Figure 9). Rupture dynamics are affected by fault roughness, particularly at the edges of the bend at the location of the closed gap between the central and eastern sections of the HFFZ. In scenarios incorporating fault roughness, rupture is partially delayed (scenario C5-R). It can also be completely arrested (scenarios C3-R and C4-R) at these locations in contrast to the reference

21699356, 2023, 6, Downloaded from https://agupubs.onlinelibrary.wiley.com/doi/10.1029/2022JB025886 by Cochrane Germany, Wiley Online Library on [20/02/2024]. See the Terms and Conditions (https://onlinelibrary.wiley.com/terms-and-conditions) on Wiley Online Library for rules of use; OA articles are governed by the applicable Creative Commons License

21699356, 2023, 6, Downloaded from https://agupubs.onlinelibrary.wiley.com/doi/10.1029/2022JB025886 by Cochrane Germany, Wiley Online Library on [20/02/2024]. See the Terms and Conditions (https://onlinelibrary.wiley.com/terms-and-conditions) on Wiley Online Library for rules of use; OA articles are governed by the applicable Creative Commons License

Table 2
Simulated Ground Motions (SA[1.0 s], g) at Selected Towns in Northern Iceland for Chosen Dynamic Rupture Earthquake Scenarios

Model	Mw	$\Delta\sigma$ (Mpa)	Húsavík	Akureyri	Dalvík	Ólafsf.	Sigluf.	Grenivík
A1	6.76	10.22	0.06	0.05	0.08	0.11	0.17	0.10
A2	6.91	10.29	0.36	0.08	0.15	0.13	0.06	0.21
A3	6.50	11.00	0.32	0.04	0.05	0.03	0.02	0.06
B1	7.145	10.80	0.60	0.04	0.05	0.04	0.04	0.08
B2	6.786	10.53	0.03	0.01	0.03	0.03	0.07	0.03
B3	7.155	11.07	0.52	0.02	0.03	0.07	0.14	0.04
B4	6.945	9.63	0.66	0.02	0.02	0.02	0.01	0.04
B5	6.944	10.93	0.79	0.02	0.04	0.03	0.03	0.05
C1	7.302	10.70	1.41	0.06	0.08	0.05	0.07	0.09
C1-R	7.250	11.38	0.79	0.05	0.09	0.05	0.05	0.09
C3	7.294	10.58	1.55	0.02	0.06	0.09	0.20	0.03
C3-R	7.031	11.56	0.03	0.01	0.03	0.05	0.15	0.02
C4	7.294	10.55	0.63	0.02	0.08	0.09	0.22	0.05
C4-R	6.869	11.38	0.46	0.02	0.01	0.01	0.01	0.01
C5	7.299	10.65	0.80	0.04	0.10	0.10	0.21	0.06
C5-R	7.245	11.24	0.72	0.05	0.08	0.09	0.21	0.08

Note. $\Delta\sigma$ represents the average stress drop across the ruptured faults.

ruptures without fault roughness. The delayed rupture is associated with a noticeable local drop in the seismic moment release rate. We highlight that if fault roughness is incorporated and all other dynamic parameters remain unchanged, scenarios based on Model-C (scenarios C3-R and C4-R) lead to smaller moment magnitudes, which are more comparable to historic magnitudes than the full HFF ruptures of Model-C scenarios without roughness (Figure 9 and Table 2). Fault roughness allows physics-based generation of high frequencies. We observe higher frequencies but lower ground motion intensities at moderate frequencies (1 s period), especially in the near-field region (Figure S9 in Supporting Information S1). Variations in high-frequency radiated spectra are expected to depend on the local rupture velocity and roughness profile (Dunham et al., 2011).

4. Synthetic Ground Motion Characteristics

The ground motion synthetics resulting from all physics-based earthquake scenarios in this study show heterogeneous distributions along and across the fault system. We resolve (dynamic) effects that are not fully accounted for in empirical ground-motion models. For near-fault motions, the simulated ground shaking intensities are strongly affected by geometric fault complexity (e.g., fault segmentation or gaps), dynamic irregularities of the propagating rupture (e.g., local acceleration and deceleration, dynamic triggering, backward-propagating fronts), forward directivity effects (see Text S3 in Supporting Information S1) and topography amplification.

Prestress remains homogeneous in all models, consistent with regional seismotectonics. Model-A's repeated rupture jumping (e.g., K. J. Ryan & Oglesby, 2014) across highly segmented faults and increased R_0 both favor local supershear rupture episodes. Given the general paucity of sustained supershear rupture in observations and models (e.g., Das, 2015; Liang et al., 2022), we refrain from analyzing ground motions for supershear rupture scenarios. This would be interesting in future work, specifically in the context of the recent submerged strike-slip supershear rupture in Palu, Sulawesi (e.g., Ulrich, Vater, et al., 2019).

4.1. Comparison With New Hybrid Bayesian Empirical Ground Motion Models

GMMs describe ground motion scaling with earthquake source properties (magnitude and faulting mechanism), source-to-site distance, and site response. They are key elements of PSHA (e.g., Field et al., 2003; Nekrasova

21699356, 2023, 6, Downloaded from https://agupubs.onlinelibrary.wiley.com/doi/10.1029/2022JB025886 by Cochrane Germany, Wiley Online Library on [20/02/2024]. See the Terms and Conditions (https://onlinelibrary.wiley.com/terms-and-conditions) on Wiley Online Library for rules of use; OA articles are governed by the applicable Creative Commons License

et al., 2014; Silva et al., 2020). The regional attenuation relationships predicted by GMMs based on observations from specific seismically active regions may not be directly applicable to other regions, of which Iceland is a prime example (see Kowsari et al., 2020, and references therein). To cope with this problem, logic tree approaches combining different regional GMMs have been used in regions where attenuation relationships are not well constrained (e.g., Bommer & Stafford, 2020; Cotton et al., 2006). However, this approach is of little use when the underlying GMMs cannot appropriately capture the salient features of the existing strong-motion data for the region. Recently, Kowsari et al. (2020) recalibrated four existing GMMs (KSea20 A/B, C, D, and E) using Bayesian inference with informative priors for key GMM parameters to model magnitude- and distance-dependent attenuation of seismic motions. They also proposed a new GMM (KSea 20 F) with a magnitude-dependent source depth term, simulating the non-self-similar magnitude scaling of the peak ground motion parameters from larger earthquakes in shallow tectonic regions. All models were constrained by Icelandic strong-motion data for the peak ground acceleration and pseudo-spectral acceleration for oscillator periods ($\leq$2.5, or 5 s) of engineering interest. The GMMs measure is RIavg (rotation invariant average of the horizontal components) which we note is essentially identical to the RotD50 measure used in our study (Kowsari et al., 2020). In the following, the GMMs serve as a baseline for the comparison of the salient features of the ground motion distribution from the physics-based rupture models in this study with those from the actual data.

The synthetic ground motions (SA[1.0 s]) from Model-B scenarios compare well with the GMMs in Kowsari et al. (2020) for scenarios with M_w greater than 6.9 in both the near- and far-fields (Figure 10a,c-e), but show lower intensity ground motions than the GMMs for smaller magnitudes in the near-field (Figure 10b). A similar agreement for the 2 s periods is shown in Figure S10 in Supporting Information S1. Rupture scenarios of similar magnitudes and involving the same faults (B1 and B3, B4 and B5) show nearly identical attenuation relationships in the near-field, even if the ground motion distribution differs significantly among scenarios. The ground motion synthetics of the four scenarios based on model-C also compare well with GMMs (Figure 11) and yield very similar average attenuation relationships, especially in the near-field region up to 20 km R_{JB} distance, despite the different ground shaking patterns they produce.

4.2. Standard Deviation of Ground Motions

The logarithmic standard deviation σ (e.g., Strasser et al., 2009) of GMMs quantifies ground motion variability (Atik et al., 2010). This may strongly impact seismic hazard assessment. σ aggregates many sources of aleatory and epistemic uncertainty and is often considered as a constant value in GMMs. Figure 12 shows the distance dependence of σ of the SA[1.0s] for the aforementioned five scenarios across Model-B (left) and four scenarios across Model-C (right). For both models, the obtained σ is on average higher than the constant intra-event variability of 0.573 from Boore and Atkinson (2008) and 0.452–0.462 from Kowsari et al. (2020) within 50 km R_{JB} distance. The standard deviations in the GMMs from Kowsari et al. (2020) are smaller. Their study region, the SISZ, is a unique seismogenic zone with repeated right-lateral strike-slip north–south striking "bookshelf" tectonic earthquakes across an approximately 80 $\times$ 20 km study region. In our study region, fault geometries and onshore and offshore environments are more complex; thus, a larger standard deviation in regional GMMs may be expected.

σ is higher in unilateral rupture scenarios (scenarios B1, B5, C1, and C5, with σ = 0.6–0.9) than in bilateral rupture scenarios (scenarios B2, B3, B4, C3, and C4, with σ = 0.5–0.7) (Figure 12). This effect also shows as a larger spread of ground motions at the same distance for the unilateral rupture scenarios in Figures 10 and 11. The intra-event variability is small near the faults ($\leq$5 km) and far away from the faults ($\geq$45 km) but differs significantly at intermediate distances, between 5 and 45 km. Figure S11 in Supporting Information S1 shows a detailed comparison between unilateral scenario Model-C1 and bilateral scenario Model-C3, particularly in the distance range of 10–15 km from the fault. These two rupture scenarios have similar magnitudes and break the same fault segments. We see lower ground motion intensity in the rupture backward direction and higher intensity in the forward direction of the unilateral rupture scenario (Figures S11c and S11d in Supporting Information S1). This stronger directivity effect increases the range of the ground motion intensity distribution (Figures S11b–S11d in Supporting Information S1) and leads to a larger σ in the unilateral rupture scenario.

We identify only small differences in σ comparing scenarios with the same rupture mode (unilateral or bilateral) and breaking the same fault segments, such as the scenarios B1 and B5, B3 and B4, C1 and C5, C3 and C4, respectively. However, when comparing scenarios with the same mode but breaking different segments, we

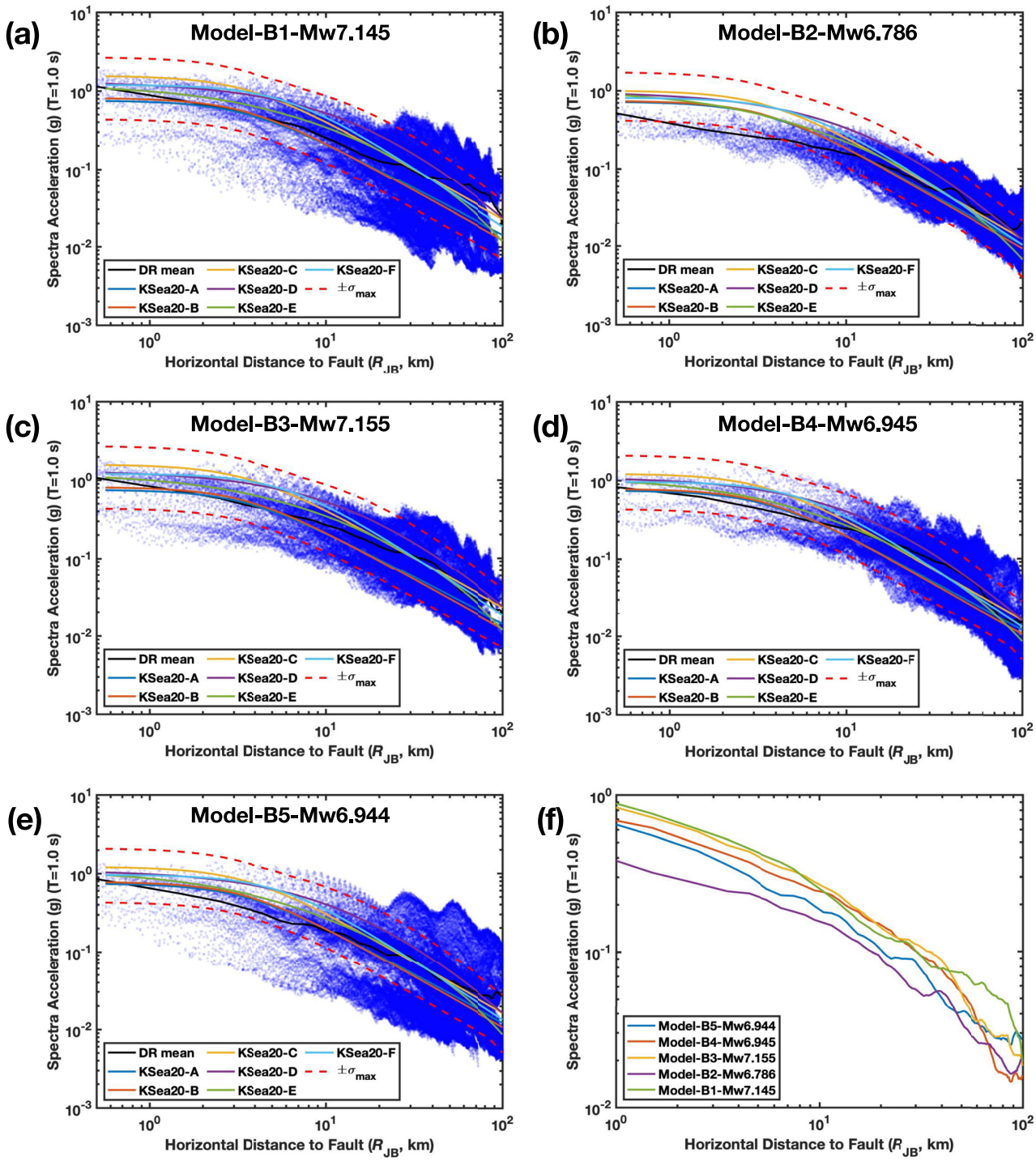

Figure 10. Comparison of the synthetic ground motion from earthquake scenarios across Model-B and ground motion models (GMMs), in terms of spectral acceleration (SA[1.0 s], in g) are presented in panels from (a)–(e). The synthetic ground motion at each cell of the triangulated ground surface output is shown by scattered blue dots. The synthetic average attenuation relationship is indicated by the black line. Colored solid lines show the mean value of each GMM for the same moment magnitude as that simulated. The dashed lines indicate the largest standard deviation value of all considered GMMs. (f) Mean attenuation relationship for the five rupture scenarios across Model-B.

21699356, 2023, 6, Downloaded from https://agupubs.onlinelibrary.wiley.com/doi/10.1029/2022JB025886 by Cochrane Germany, Wiley Online Library on [20/02/2024]. See the Terms and Conditions (https://onlinelibrary.wiley.com/terms-and-conditions) on Wiley Online Library for rules of use; OA articles are governed by the applicable Creative Commons License

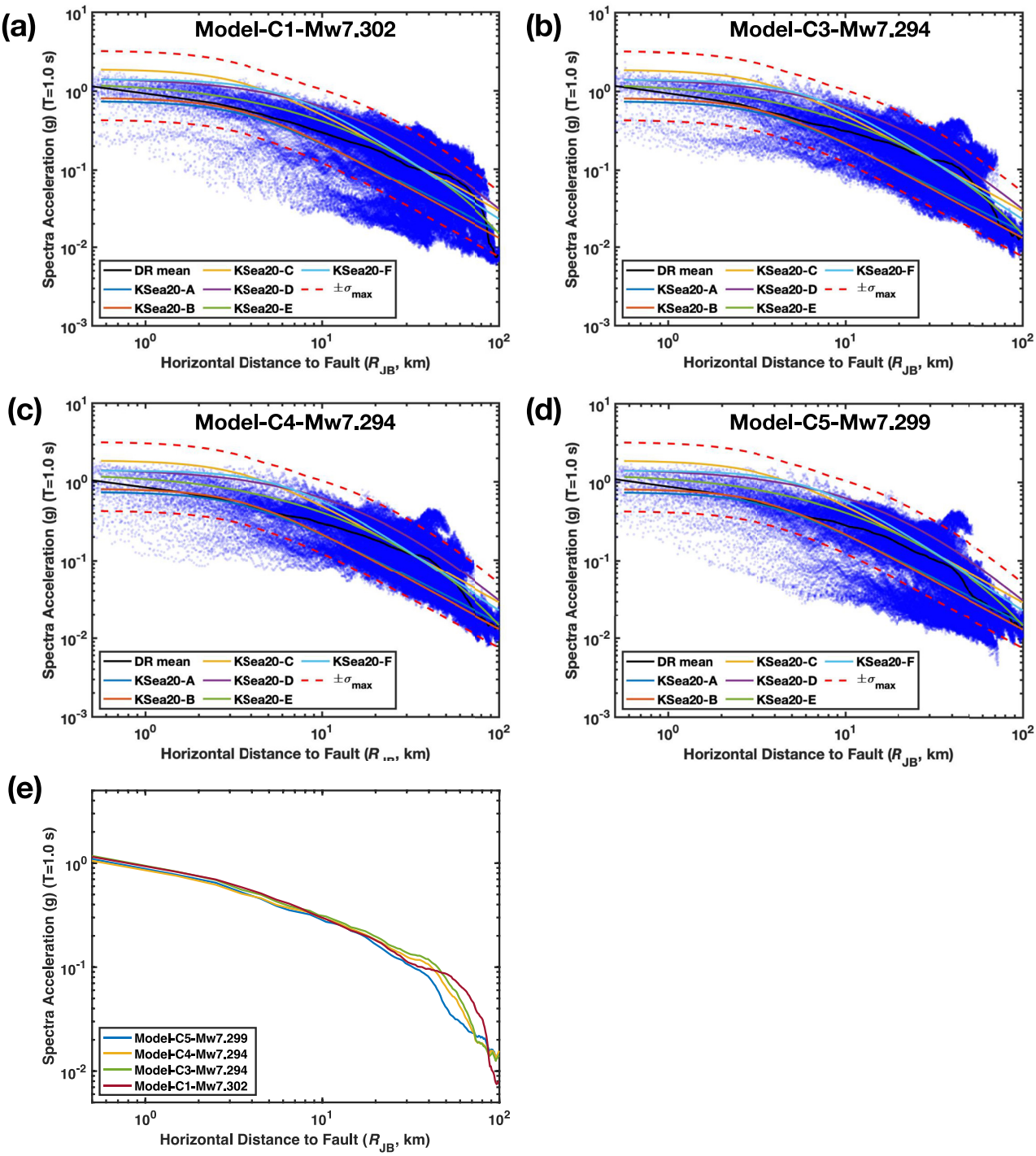

Figure 11. (a)–(e) Comparison of the synthetic ground motion from earthquake scenarios across Model-C and ground motion models in terms of spectral acceleration (SA[1.0 s], in g). See the caption of Figure 10 for further details. (e) Mean attenuation relationship for the four rupture scenarios across Model-C.

observe a larger σ difference. For example, scenarios B2 and B3 are both bilateral, but B2 breaks Western branch fault segments whereas B3 ruptures the main fault segment (Figure 6). This results in a lower σ in the range of 0.35–0.42 for B2, while B3 has a larger σ of 0.56–0.7 (Figure 12). This indicates that local fault geometry, velocity structure, and topography/bathymetry can modulate ground motions but not as effective as the rupture mode. We conclude that the observed intra-event variability (distance and rupture mode dependent) is a robust

21699356, 2023, 6, Downloaded from https://agupubs.onlinelibrary.wiley.com/doi/10.1029/2022JB025886 by Cochrane Germany, Wiley Online Library on [20/02/2024]. See the Terms and Conditions (https://onlinelibrary.wiley.com/terms-and-conditions) on Wiley Online Library for rules of use; OA articles are governed by the applicable Creative Commons License

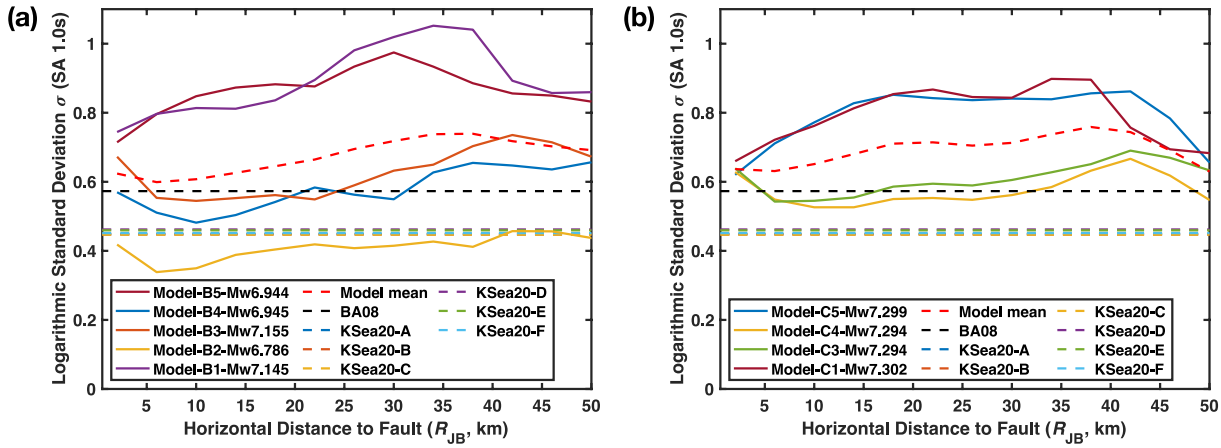

Figure 12. Variation with source R_{JB} distance of the (logarithmic) standard deviation of the ground motion synthetics (spectral acceleration SA[1.0 s] in g) for Model-B (a) and Model-C (b) compared with other ground motion models (GMMs). The standard deviation of each scenario (intra-event standard deviation) is plotted using solid lines of different colors. The red dashed line shows the mean standard deviation and the black dashed line is the constant standard deviation (0.573) inferred by Boore and Atkinson (2008). Other dashed color lines denote the constant standard deviation of the GMMs by Kowsari et al. (2020).

result in our physics-based models, which is distinct from the typically constant intra-event variability shown in empirical GMMs.

In Table 2, we list the simulated ground shaking (SA[1.0 s]) for seven towns from earthquake scenarios based on all three geometry models. All three models exhibit a similar mean stress drop. Scenarios with fault roughness generate a slightly higher mean stress drop of ~11.4 MPa. The higher R_0 prescribed in Model-A does not translate into larger mean stress drop values, balanced by other dynamic parameters (see Section 2.3). On average, the rupturing faults are less optimally oriented in Model-A than in Model-B and Model-C (Figure S12 in Supporting Information S1). In addition, Model-A assumes a slightly higher fluid pressure ratio which reduces the stress drop.

Húsavík, the second largest town in this area, is located on the eastern segment of the HFFZ and experiences in most scenarios the strongest ground shaking. Among all simulated scenarios, the strongest ground motion at Húsavík town is SA[1.0 s] = ~1.55 g for the M_w7.3 scenario C3. Scenario C3 is nucleated in the central section of the HFFZ and breaks the entire main fault. At Húsavík, M_w7.3 scenarios C4 and C5 and M_w6.9 scenarios B4 and B5 generate similar levels of ground shaking, despite their differing earthquake magnitudes. This suggests that for such large earthquakes, a small portion of the ruptured faults can locally dominate near-field ground shaking. Previous observational and theoretical studies suggest that the peak ground motion amplitudes in forward directivity of shallow, crustal earthquakes are dominated by the seismic radiation of a limited portion of the fault plane (Halldorsson & Papageorgiou, 2012; Spudich & Chiou, 2008; Spudich et al., 2004). This leads to a deviation from self-similar amplitude scaling of near-fault peak motions and is so prevalent that GMMs that do not account for such saturation of near-fault motions do not satisfy the established criteria for use in PSHA (Bommer et al., 2010; Cotton et al., 2006; Kowsari et al., 2020). Scenario A2, of similar magnitude as scenarios B4 and B5, generates weaker ground shaking in Húsavík, possibly due to smaller peak slip rates on the eastern section of the HFFZ, combined with weaker directivity effects associated with shorter fault segments (Wang & Day, 2020). However, scenarios based on Model-A result in stronger ground shaking than Model-B and Model-C in other towns further away from the fault system, especially in Dalvík, Ólafsfjörður, and Grenivík. All scenarios incorporate the same 3-D velocity structure and topography/bathymetry but differ in their dynamic source effects. We speculate that the differences in ground motion intensity may be due to the stronger seismic radiation emanating from segments hosting supershear ruptures that can transmit larger amplitude ground motion to locations far from the fault (Dunham & Bhat, 2008) and from local decelerating and accelerating slip during rupture jumping episodes (e.g., Oglesby & Mai, 2012). The ground shaking of scenarios with roughness (scenarios C1-R and C5-R) at Húsavík is weaker than in the reference scenarios without roughness (scenarios C1 and C5) by about a factor of 2 for scenario C1. This may be a consequence of less-coherent signals from small and localized radiation (Graves & Pitarka, 2016).

21699356, 2023, 6, Downloaded from https://agupubs.onlinelibrary.wiley.com/doi/10.1029/2022JB025886 by Cochrane Germany, Wiley Online Library on [20/02/2024]. See the Terms and Conditions (https://onlinelibrary.wiley.com/terms-and-conditions) on Wiley Online Library for rules of use; OA articles are governed by the applicable Creative Commons License

21699356, 2023, 6, Downloaded from https://agupubs.onlinelibrary.wiley.com/doi/10.1029/2022JB025886 by Cochrane Germany, Wiley Online Library on [20/02/2024]. See the Terms and Conditions (https://onlinelibrary.wiley.com/terms-and-conditions) on Wiley Online Library for rules of use; OA articles are governed by the applicable Creative Commons License

5. Discussion

In this study, we develop a series of mechanically plausible dynamic rupture scenarios on the HFFZ, the largest strike-slip fault in Iceland using recent geophysical observations. We analyze the modeled ground motions and verify them by comparison to the latest empirical GMMs (Kowsari et al., 2020). We discuss future physics-based constraints on long-period seismic hazard, particularly in the near-fault region. We include bathymetry constrained by high-resolution imaging and a high-resolution 3-D velocity model (Abril et al., 2021; Brandsdóttir et al., 2005; Einarsson & Brandsdóttir, 2021; Magnúsdóttir et al., 2015). We keep topo-bathymetry and the 3-D velocity model unchanged in our simulations in order to isolate the relative effects of fault geometry, which is less well-constrained. Quantifying site-specific effects of only topo-bathymetry would require simulations with a flat free surface and isolation of the 3-D heterogeneous velocity structure effect, which are not considered here given the well-constrained character of this data set.

Our dynamic rupture simulations demonstrate that the fault system geometry, hypocenter location, and initial stress conditions strongly affect earthquake rupture dynamics, slip amplitude and distribution, and the moment magnitude of the fully dynamic scenarios in the HFFZ. The level of complexity of the assumed fault model is a key parameter constraining the final magnitude of our earthquake scenarios, their rupture duration, and dynamic complexity.

Scenarios using the complex Model-A, with its 55 fault segments separated by various gaps and step-overs, rupture a significant portion of the whole HFFZ. However, the high segmentation of Model-A does not favor rupture scenarios that result in earthquakes larger than M_w7. The Model-A dynamic parameters required for sustained earthquake scenarios of realistic magnitude (Table 1) promote direct branching and dynamic triggering (rupture jumping) and, therefore, multi-fault earthquake rupture. We observe forward and backward propagating ruptures of adjacent segments and episodes of localized supershear rupture velocity (Figure 2). In Model-A scenarios, fault slip distributions are highly heterogeneous. Similar dynamic complexities have been inferred in data-constrained multi-fault dynamic rupture models of well-recorded events, such as the 1992 multi-segment strike-slip Landers, California, earthquake (Wollherr et al., 2019).

In contrast, the less segmented fault systems of Model-B and Model-C are dynamically able to generate M_w7+ rupture scenarios. The prominent ∼4 km wide compressional step over between the eastern and central sections of the HFFZ incorporated in Model-B represents a strong dynamic barrier, effectively limiting rupture propagation of all our Model-B earthquake scenarios and their magnitudes to M_w6.9–7.1. This is not unexpected: field observations and numerical studies suggest that strike-slip earthquake rupture rarely jumps across step-overs wider than a few kilometers, especially for compressional step-overs (Elliott et al., 2009; Oglesby, 2005; Wesnousky, 1988). Closing the geometric gap in model-C scenarios however leads to through-going rupture breaking the complete main fault, resulting in M_w ∼7.3 rupture scenarios.

None of our scenarios based on Model-B and Model-C show dynamic triggering between the main fault and the secondary faults of the western HFFZ. The dynamic stress ahead of a westwards propagating rupture front across the right lateral main fault clamps the southern fault and unclamps the northern fault. The northern fault is not activated in any of our scenarios due to a ∼2 km wide gap separating it from the main fault. The southern fault segments are unclamped when rupture nucleates on the west segment and propagates to the east. But the obtuse angle the southern fault forms with the eastward rupture propagation does not favor dynamic triggering. The dynamic stresses generated by an eastwards propagating rupture of the main fault results in left-lateral shear stressing of the Southern fault (e.g., Poliakov et al., 2002) in contrast to the right-lateral initial shear stress loading this segment due to the regional stress field.

Fliss et al. (2005) propose a mechanism for "backward branching" of secondary faults that form an obtuse angle with the direction of 2-D mode II rupture propagation. They suggest that intense stress radiation from rupture arrest on the main fault can dynamically trigger a neighboring secondary fault in such specific configurations, which can then rupture bilaterally. In Model-B and Model-C, the unsegmented main fault geometry does not offer strong barriers aiding the backward triggering of secondary faults of the western HFFZ. We do observe backward branching using Model-A, for instance in scenario A2. Spontaneous rupture arrest on the eastern edge of segment F30 allows rupture jumping to segment F33. New rupture dynamically initiates centrally on F33, which is close to the eastern edge of F30, and propagates bilaterally (Figure 2a) in agreement with earlier 2D analysis (Fliss et al., 2005).

21699356, 2023, 6, Downloaded from https://agupubs.onlinelibrary.wiley.com/doi/10.1029/2022JB025886 by Cochrane Germany, Wiley Online Library on [20/02/2024]. See the Terms and Conditions (https://onlinelibrary.wiley.com/terms-and-conditions) on Wiley Online Library for rules of use; OA articles are governed by the applicable Creative Commons License

Varying hypocenter locations can affect the final slip distribution and magnitude, as well as the spatio-temporal evolution of earthquake rupture, but the strength of this effect depends on fault geometry. In all scenarios based on the complex geometry of Model-A, only a few fault segments in the hypocentral region rupture. Scenarios of magnitude M_w6.76, M_w6.91, and M_w6.50 are obtained for hypocenters in the west, central, and east of the HFFZ, respectively (Figure 3). The variation of hypocenter location on the well-connected faults of Model-B has only a minor effect on the final magnitude: M_w7.145 and M_w7.155 for scenarios B1 and B3, M_w6.945 and M_w6.944 for scenarios B4 and B5. The slip distributions are significantly modulated by hypocenter location, with larger slip at greater distances from the hypocenter.

Scenarios with different hypocenters differ in their kinematic properties. For instance, scenario B3 has slower rupture propagation in the central segment than scenario B1 (Figure 5). The effect of the hypocenter location on the spatial-temporal evolution of the earthquake rupture is also noticeable in Model-C scenarios. Rupture transition from the eastern to the central section of the HFFZ is delayed in scenario C4, which is nucleated at the main fault bend near the now closed gap on the eastern section of the HFFZ (Figure 7). When the hypocenter is far from the fault bend, rupture can propagate smoothly across it. Similar hypocenter location effects have been observed in previous finite-source models and dynamic studies for different fault networks (e.g., P. M. Mai et al., 2005; Oglesby & Mai, 2012; Kyriakopoulos et al., 2019).

The smooth main fault bend in Model-C scenarios does allow some ruptures to propagate across while terminating others depending on the local prestress and dynamic stress evolution. The bend is a so-called "earthquake gate" (e.g., Liu et al., 2021, 2022). The segmented, explicitly modeled geometrical barrier posed by the open gap in our Model-B scenarios, however, is different and can effectively stop all dynamically plausible rupture scenarios. This highlights the importance of acknowledging segmented fault system geometries when studying earthquake gates such as the Big Bend or the Cajon Pass of the Southern San Andreas fault and the Nothern San Jacinto fault (Lozos, 2016), respectively.

The effect of fault geometry and hypocenter location on earthquake rupture evolution and magnitude of rupture scenarios is dependent on the initial stress conditions (see Text S2 in Supporting Information S1). Our sensitivity analysis of the prestress-related initial parameters–SH_{max}, $s2_{ratio}$, γ, and R_0, show that rupture transitions between multiple segments of the main fault are differently affected by fault geometry and hypocenter location depending on the initial dynamic parameters (Figures S13, S14, S15, and S16 in Supporting Information S1). Our sensitivity analysis demonstrates that the non-linearity relating initial conditions to fault geometry renders 3-D complex dynamic rupture simulations an indispensable tool for fully physics-based earthquake scenarios and ground motion modeling.

Future extensions of our study may address the challenges in observationally constraining our earthquake scenarios. Specifically, the variability of the locking depth, the connection or disconnection between fault segments, and the 3-D variability of fault stress and strength are poorly constrained. We here assume in all models a purely strike-slip loading and depth-dependent background stress and fault strength parameters and omit potential additional along-strike heterogeneity. However, our effective fault prestress is 3-D heterogeneous due to the modulation by fault geometry.

Due to the offshore location of the mostly submerged fault system and limited data coverage, the locking depth of HFFZ is poorly constrained. Seismic-tectonic analysis of Rögnvaldsson et al. (1998) suggests a locking depth of 10–12 km in the TFZ, and geodetic global navigation satellite system (GNSS) analyses indicate a shallower locking depth of 5 km (Árnadóttir et al., 2009) or $6.3^{+1.7}_{-1.2}$ km (Metzger et al., 2011), or 6–10 km using combined GNSS and InSAR data (Metzger & Jónsson, 2014). The lower thermal gradients in the west of the HFFZ may be associated with local variations of the locking depth. The seismogenic depth could decrease from west to east (Flóvenz & Saemundsson, 1993; Metzger et al., 2011). Here, we smoothly taper deviatoric stresses below 9 km depth over 2 km without lateral variations. Future models may study the effects of a variation of locking depth on rupture dynamics, slip amplitude, earthquake magnitude and ground shaking (e.g., Kyriakopoulos et al., 2019; Oglesby, 2020; Smith-Konter & Sandwell, 2009). However, we expect that our main conclusions on the relative effects of fault geometry, hypocenter locations (rupture directivity), and topography on rupture dynamics and ground shaking in the HFFZ will remain valid with a different locking depth.

We model the HFFZ with both a complex fault geometry (Model-A) consisting of 55 fault segments and two more simple fault geometries (Model-B and Model-C) consisting of 4 or 3 faults. It is possible that the actual

21699356, 2023, 6, Downloaded from https://agupubs.onlinelibrary.wiley.com/doi/10.1029/2022JB025886 by Cochrane Germany, Wiley Online Library on [20/02/2024]. See the Terms and Conditions (https://onlinelibrary.wiley.com/terms-and-conditions) on Wiley Online Library for rules of use; OA articles are governed by the applicable Creative Commons License

fault system geometry falls in between or shows discontinuities at the surface but a highly connected geometry at depth, as it has been suggested for other mature fault networks (e.g., Elliott et al., 2009), motivating further analysis of fault geometry effects. Our assumed regional, depth-dependent prestress results in similar stress conditions for similarly oriented fault segments. However, Passarelli et al. (2018) infer normal faulting focal mechanisms in the western HFFZ. Heterogeneous fault stresses unrelated to fault geometry may build up throughout the long-term seismic cycle, specifically in fault systems featuring stark geometric complexities and step-overs (Duan & Oglesby, 2006). These effects may be captured in a future combination of dynamic rupture scenarios with seismic cycle simulations (e.g., Galvez et al., 2020).

Our dynamic rupture simulations can complement GMM-based approaches for assessing the seismic hazard in the HFFZ. Our synthetic ground motions agree well with the GMMs developed from data in the tectonically and seismically symmetric SISZ (Kowsari et al., 2020) in terms of their average attenuation relationships (Figures 10 and 11). In addition, the average ground motions show magnitude-consistent attenuation relationships in our synthetic scenarios when breaking the same fault segments. This makes it possible to derive a physics-based GMM from physics-based simulation data only or combined with empirical data. Such GMMs could improve near-field ground motion predictions and narrow down the extreme ground motion limits predicted by empirical GMMs, making the GMMs more effective and reliable tools for use in PSHA. Also, our dynamic rupture scenarios can match the inferred characteristics of historical events, such as moment magnitude and rupture extent (Section 3.1). An important advantage of dynamic rupture scenario based ground motion modeling is the physically realistic source description. The synthetic ground motion accounts realistically and self-consistently for complex path effects within 3-D velocity structure, source directivity, and local site conditions (basin effects, topography, and bathymetry). Fully considering shallow site effects may further amplify the high-frequency content of our synthetics (e.g., Rodgers et al., 2020). Finally, the physics-based approach of this study may be applied to other regions with limited seismic databases but known earthquake faults.

6. Conclusion

We present physics-based earthquake scenarios on the HFFZ based on 3-D spontaneous dynamic rupture simulations. Our scenarios incorporate a regional 3-D velocity structure, fault complexity, bathymetry, topography, off-fault plasticity, and viscoelastic attenuation. We vary the segmented fault system geometry and potential hypocenter locations in a suite of earthquake scenarios, which vary in earthquake magnitude, fault slip, and the spatiotemporal evolution of rupture dynamics. We find highly variable ground motions that differ spatially and across the scenarios. We consider three fault system geometries with different complexity. All three fault geometries can spontaneously produce fully dynamic earthquake scenarios of comparable magnitudes to historic events when combined with simple observationally constrained tectonic background stress and depth-dependent loading. The most complex fault system, Model-A, consists of 55 vertical faults of varying sizes and orientations that are separated by gaps of different widths. This highly segmented geometry does not allow a model of dynamically viable and realistic M_w7+ scenarios. Our Model-A scenarios feature highly complex rupture dynamics, including branching, dynamic triggering, supershear rupture speeds, and reverse slip, but rupture only parts of the HFFZ.

The less-segmented Model-B and Model-C fault geometries can host sustained dynamic ruptures along the well-connected main fault segments. The open gap in Model-B acts as a strong barrier preventing dynamic triggering (rupture jumping), leading to scenarios with magnitudes up to M_w7.15. Model-C can host rupture scenarios up to M_w7.3, which ruptures the entire main fault. Fault roughness can significantly affect rupture dynamics and physically plausible maximum magnitudes by delaying or arresting rupture propagation.

All simulated scenarios yield heterogeneous ground motion distributions. We show detailed ground motion analysis from comparable Model-B and -C dynamic rupture scenarios. We observe ground shaking amplification from rupture directivity, localized geometric complexities, such as fault gaps and bends, and topography which can modulate ground motion variability. The coupled effects of rupture directivity and fault geometry generate narrow bands with amplified ground motion. Among all analyzed scenarios, the strongest ground motion at Húsavík is SA[1.0 s] = ∼1.55 g.

The modeled average ground-motion attenuation characteristics are nearly identical and independent of the analyzed variations in source complexity. The physics-based ground motions we generate (quantified by SA[1.0s]) show good agreement with the distance attenuation predicted by the latest GMMs for Iceland and are magnitude

21699356, 2023, 6, Downloaded from https://agupubs.onlinelibrary.wiley.com/doi/10.1029/2022JB025886 by Cochrane Germany, Wiley Online Library on [20/02/2024]. See the Terms and Conditions (https://onlinelibrary.wiley.com/terms-and-conditions) on Wiley Online Library for rules of use; OA articles are governed by the applicable Creative Commons License

consistent when breaking the same fault segments. We show that the modeled ground motion variability changes with distance to the fault and is larger for unilateral rupture scenarios than for bilateral rupture scenarios. On average, variability is higher than the typically (constant) standard variation assumed in empirical GMMs.

Assuming simple prestress and complex fault geometries, dynamic effects such as rupture directivity can change ground motions locally, which may be captured in future GMMs, including physics-based modeling. Hybrid or purely physics-based GMMs may readily complement regional hazard analysis, specifically regarding inter- and intra-event variability and site-specific hazard assessments. We conclude that ensembles of physics-based and observationally informed earthquake scenarios can complement empirical seismic hazard assessment methods. Dynamic rupture simulations can characterize the hazard of tectonically and seismically complex regions, such as the multi-fault HFFZ in Northern Iceland, especially when instrumental data are limited.

Data Availability Statement

We use the open-source software package SeisSol, available at https://github.com/SeisSol/SeisSol. Input files required to run all dynamic rupture simulations shown in the study can be downloaded from https://zenodo.org/record/7990543. The structural model incorporates topography and bathymetry data from GeoMapApp (www.geomapapp.org)/(W. B. Ryan et al., 2009).

Acknowledgments
This work received funding from the European Union's Horizon 2020 research and innovation programme (TEAR ERC Starting grant agreement Nos. 823844 and 852992) and Horizon Europe (ChEESE-2P Grant 101093038, DT-GEO Grant 101058129, and Geo-INQUIRE Grant 101058518). We acknowledge additional funding from the National Science Foundation (Grant EAR-2121666), the National Aeronautics and Space Administration (80NSSC20K0495), the Southern California Earthquake Center (SCEC awards 23121, 22135), the Icelandic Research Fund (SENSHAZ, Grant 196089) and King Abdullah University of Science and Technology (KAUST, Grant BAS/1/1339-01-01). We are thankful to Bryndis Brandsdóttir at the University of Iceland for providing the mapping data for the complex fault trace. The authors acknowledge the Gauss Centre for Supercomputing e.V. (www.gauss-centre.eu, project pr63qo) for funding this project by providing computing time on the GCS Supercomputer SuperMUC-NG at Leibniz Supercomputing Centre (www.lrz.de). Computing resources were also provided by the Institute of Geophysics of LMU Munich (Oeser et al., 2006).

References

Abercrombie, R. E., & Ekström, G. (2001). Earthquake slip on oceanic transform faults. *Nature*, *410*(6824), 74–77. https://doi.org/10.1038/35065064

Abril, C., & Gudmundsson, O., & the SIL Seismological Group. (2018). Relocating earthquakes with empirical traveltimes. *Geophysical Journal International*, *214*(3), 2098–2114. https://doi.org/10.1093/gji/ggy246

Abril, C., Guðmundsson, O., & Tryggvason, A., & the SIL Seismological Group. (2019). Earthquake relocation in the Tjörnes Fracture Zone. In *Proceedings of the international workshop on earthquakes in North Iceland*, Húsavík, Iceland.

Abril, C., Tryggvason, A., Gudmundsson, Ó., & Steffen, R. (2021). Local earthquake tomography in the Tjörnes Fracture Zone (North Iceland). *Journal of Geophysical Research: Solid Earth*, *126*(6). https://doi.org/10.1029/2020jb020212

Aderhold, K., & Abercrombie, R. E. (2016). The 2015 M_W 7.1 earthquake on the Charlie-Gibbs transform fault: Repeating earthquakes and multimodal slip on a slow oceanic transform. *Geophysical Research Letters*, *43*(12), 6119–6128. https://doi.org/10.1002/2016gl068802

Ando, R., & Kaneko, Y. (2018). Dynamic rupture simulation reproduces spontaneous multifault rupture and arrest during the 2016 M_W 7.9 Kaikoura earthquake. *Geophysical Research Letters*, *45*(23), 12875–12883. https://doi.org/10.1029/2018GL080550

Andrews, D. (1976). Rupture velocity of plane strain shear cracks. *Journal of Geophysical Research*, *81*(32), 5679–5687. https://doi.org/10.1029/jb081i032p05679

Angelier, J., Slunga, R., Bergerat, F., Stefansson, R., & Homberg, C. (2004). Perturbation of stress and oceanic rift extension across transform faults shown by earthquake focal mechanisms in Iceland. *Earth and Planetary Science Letters*, *219*(3–4), 271–284. https://doi.org/10.1016/s0012-821x(03)00704-0

Aochi, H., & Madariaga, R. (2003). The 1999 Izmit, Turkey, earthquake: Nonplanar fault structure, dynamic rupture process, and strong ground motion. *Bulletin of the Seismological Society of America*, *93*(3), 1249–1266. https://doi.org/10.1785/0120020167

Árnadóttir, T., Lund, B., Jiang, W., Geirsson, H., Björnsson, H., Einarsson, P., & Sigurdsson, T. (2009). Glacial rebound and plate spreading: Results from the first countrywide GPS observations in Iceland. *Geophysical Journal International*, *177*(2), 691–716. https://doi.org/10.1111/j.1365-246x.2008.04059.x

Atik, L. A., Abrahamson, N., Bommer, J. J., Scherbaum, F., Cotton, F., & Kuehn, N. (2010). The variability of ground-motion prediction models and its components. *Seismological Research Letters*, *81*(5), 794–801. https://doi.org/10.1785/gssrl.81.5.794

Bayat, F., Kowsari, M., & Halldorsson, B. (2022). A new 3-D finite-fault model of the Southwest Iceland bookshelf transform zone. *Geophysical Journal International*, *231*(3), 1618–1633. https://doi.org/10.1093/gji/ggac272

Ben-Zion, Y., & Sammis, C. G. (2003). Characterization of fault zones. *Pure and Applied Geophysics*, *160*(3), 677–715. https://doi.org/10.1007/pl00012554

Beroza, G. C., & Spudich, P. (1988). Linearized inversion for fault rupture behavior: Application to the 1984 Morgan Hill, California, earthquake. *Journal of Geophysical Research*, *93*(B6), 6275–6296. https://doi.org/10.1029/jb093ib06p06275

Bistacchi, A., Griffith, W. A., Smith, S. A., Di Toro, G., Jones, R., & Nielsen, S. (2011). Fault roughness at seismogenic depths from lidar and photogrammetric analysis. *Pure and Applied Geophysics*, *168*(12), 2345–2363. https://doi.org/10.1007/s00024-011-0301-7

Bommer, J. J., Douglas, J., Scherbaum, F., Cotton, F., Bungum, H., & Fah, D. (2010). On the selection of ground-motion prediction equations for seismic hazard analysis. *Seismological Research Letters*, *81*(5), 783–793. https://doi.org/10.1785/gssrl.81.5.783

Bommer, J. J., & Stafford, P. J. (2020). Selecting ground-motion models for site-specific PSHA: Adaptability versus applicability. *Bulletin of the Seismological Society of America*, *110*(6), 2801–2815. https://doi.org/10.1785/0120200171

Boore, D. M., & Atkinson, G. M. (2008). Ground-motion prediction equations for the average horizontal component of PGA, PGV, and 5%-damped PSA at spectral periods between 0.01 s and 10.0 s. *Earthquake Spectra*, *24*(1), 99–138. https://doi.org/10.1193/1.2830434

Boore, D. M., Watson-Lamprey, J., & Abrahamson, N. A. (2006). Orientation-independent measures of ground motion. *Bulletin of the Seismological Society of America*, *96*(4A), 1502–1511. https://doi.org/10.1785/0120050209

Bradley, B. A. (2012). Empirical correlations between peak ground velocity and spectrum-based intensity measures. *Earthquake Spectra*, *28*(1), 17–35. https://doi.org/10.1193/1.3675582

Brandsdóttir, B., Riedel, C., Richter, B., Helgadóttir, G., Kjartansson, E., Detrick, R., et al. (2005). *Multibeam bathymetric maps of the Kolbeinsey Ridge and Tjörnes Fracture Zone, N-Iceland*. EGU General Assembly.

Breuer, A., & Heinecke, A. (2022). Next-generation local time stepping for the ADER-DG finite element method. In *2022 IEEE international parallel and distributed processing symposium (IPDPS)* (pp. 402–413).

Bruhat, L., Klinger, Y., Vallage, A., & Dunham, E. M. (2020). Influence of fault roughness on surface displacement: From numerical simulations to coseismic slip distributions. *Geophysical Journal International*, *220*(3), 1857–1877. https://doi.org/10.1093/gji/ggz545

Byerlee, J. (1978). Friction of rocks. In *Rock friction and earthquake prediction* (pp. 615–626). Springer.
Candela, T., Renard, F., Bouchon, M., Brouste, A., Marsan, D., Schmittbuhl, J., & Voisin, C. (2009). Characterization of fault roughness at various scales: Implications of three-dimensional high resolution topography measurements. In *Mechanics, structure and evolution of fault zones* (pp. 1817–1851). Springer.
Cotton, F., Scherbaum, F., Bommer, J. J., & Bungum, H. (2006). Criteria for selecting and adjusting ground-motion models for specific target regions: Application to central Europe and rock sites. *Journal of Seismology*, *10*(2), 137–156. https://doi.org/10.1007/s10950-005-9006-7
D'Amico, V., Albarello, D., Sigbjörnsson, R., & Rupakhety, R. (2016). Seismic hazard assessment for Iceland in terms of macroseismic intensity using a site approach. *Bulletin of Earthquake Engineering*, *14*(7), 1797–1811. https://doi.org/10.1007/s10518-015-9805-3
Darbyshire, F. A., White, R. S., & Priestley, K. F. (2000). Structure of the crust and uppermost mantle of Iceland from a combined seismic and gravity study. *Earth and Planetary Science Letters*, *181*(3), 409–428. https://doi.org/10.1016/s0012-821x(00)00206-5
Das, S. (2015). Supershear earthquake ruptures–theory, methods, laboratory experiments and fault superhighways: An update. *Perspectives on European Earthquake Engineering and Seismology*, *2*, 1–20.
Das, S., & Aki, K. (1977). Fault plane with barriers: A versatile earthquake model. *Journal of Geophysical Research*, *82*(36), 5658–5670. https://doi.org/10.1029/jb082i036p05658
Dieterich, J. H., & Smith, D. E. (2009). Nonplanar faults: Mechanics of slip and off-fault damage. In *Mechanics, structure and evolution of fault zones* (pp. 1799–1815). Springer.
Di Toro, G., Han, R., Hirose, T., De Paola, N., Nielsen, S., Mizoguchi, K., et al. (2011). Fault lubrication during earthquakes. *Nature*, *471*(7339), 494–498. https://doi.org/10.1038/nature09838
Dolan, J. F., & Haravitch, B. D. (2014). How well do surface slip measurements track slip at depth in large strike-slip earthquakes? The importance of fault structural maturity in controlling on-fault slip versus off-fault surface deformation. *Earth and Planetary Science Letters*, *388*, 38–47. https://doi.org/10.1016/j.epsl.2013.11.043
Duan, B., & Oglesby, D. D. (2006). Heterogeneous fault stresses from previous earthquakes and the effect on dynamics of parallel strike-slip faults. *Journal of Geophysical Research*, *111*(B5). https://doi.org/10.1029/2005jb004138
Dunham, E. M. (2005). Dissipative interface waves and the transient response of a three-dimensional sliding interface with Coulomb friction. *Journal of the Mechanics and Physics of Solids*, *53*(2), 327–357. https://doi.org/10.1016/j.jmps.2004.07.003
Dunham, E. M., Belanger, D., Cong, L., & Kozdon, J. E. (2011). Earthquake ruptures with strongly rate-weakening friction and off-fault plasticity, Part 2: Nonplanar faults. *Bulletin of the Seismological Society of America*, *101*(5), 2308–2322. https://doi.org/10.1785/0120100076
Dunham, E. M., & Bhat, H. S. (2008). Attenuation of radiated ground motion and stresses from three-dimensional supershear ruptures. *Journal of Geophysical Research*, *113*(B8). https://doi.org/10.1029/2007jb005182
Einarsson, P. (1991). Earthquakes and present-day tectonism in Iceland. *Tectonophysics*, *189*(1–4), 261–279. https://doi.org/10.1016/0040-1951(91)90501-i
Einarsson, P. (2008). Plate boundaries, rifts and transforms in Iceland. *Jökull Journal*, *58*(12), 35–58. https://doi.org/10.33799/jokull2008.58.035
Einarsson, P., & Brandsdóttir, B. (2021). Seismicity of the northern volcanic zone of Iceland. *Frontiers of Earth Science*, *9*, 628967. https://doi.org/10.3389/feart.2021.628967
Elliott, A., Dolan, J., & Oglesby, D. (2009). Evidence from coseismic slip gradients for dynamic control on rupture propagation and arrest through stepovers. *Journal of Geophysical Research*, *114*(B2), B02313. https://doi.org/10.1029/2008jb005969
Fang, Z., & Dunham, E. M. (2013). Additional shear resistance from fault roughness and stress levels on geometrically complex faults. *Journal of Geophysical Research: Solid Earth*, *118*(7), 3642–3654. https://doi.org/10.1002/jgrb.50262
Field, E. H., Jordan, T. H., & Cornell, C. A. (2003). OpenSHA: A developing community-modeling environment for seismic hazard analysis. *Seismological Research Letters*, *74*(4), 406–419. https://doi.org/10.1785/gssrl.74.4.406
Fliss, S., Bhat, H. S., Dmowska, R., & Rice, J. R. (2005). Fault branching and rupture directivity. *Journal of Geophysical Research*, *110*(B6), B06312. https://doi.org/10.1029/2004jb003368
Flóvenz, Ó. G., & Saemundsson, K. (1993). Heat flow and geothermal processes in Iceland. *Tectonophysics*, *225*(1–2), 123–138. https://doi.org/10.1016/0040-1951(93)90253-g
Gallovič, F., Valentová, L., Ampuero, J.-P., & Gabriel, A.-A. (2019). Bayesian dynamic finite-fault inversion: 2. Application to the 2016 M_W 6.2 Amatrice, Italy, earthquake. *Journal of Geophysical Research: Solid Earth*, *124*(7), 6970–6988. https://doi.org/10.1029/2019jb017512
Galvez, P., Somerville, P., Petukhin, A., Ampuero, J.-P., & Peter, D. (2020). Earthquake cycle modelling of multi-segmented faults: Dynamic rupture and ground motion simulation of the 1992 M_W 7.3 landers earthquake. *Pure and Applied Geophysics*, *177*(5), 2163–2179. https://doi.org/10.1007/s00024-019-02228-x
Graves, R., Jordan, T. H., Callaghan, S., Deelman, E., Field, E., Juve, G., et al. (2011). CyberShake: A physics-based seismic hazard model for southern California. *Pure and Applied Geophysics*, *168*(3), 367–381. https://doi.org/10.1007/s00024-010-0161-6
Graves, R., & Pitarka, A. (2016). Kinematic ground-motion simulations on rough faults including effects of 3D stochastic velocity perturbations. *Bulletin of the Seismological Society of America*, *106*(5), 2136–2153. https://doi.org/10.1785/0120160088
Guatteri, M., Mai, P. M., & Beroza, G. C. (2004). A pseudo-dynamic approximation to dynamic rupture models for strong ground motion prediction. *Bulletin of the Seismological Society of America*, *94*(6), 2051–2063. https://doi.org/10.1785/0120040037
Guatteri, M., Mai, P. M., Beroza, G. C., & Boatwright, J. (2003). Strong ground-motion prediction from stochastic-dynamic source models. *Bulletin of the Seismological Society of America*, *93*(1), 301–313. https://doi.org/10.1785/0120020006
Halldórsson, B. (2019). Towards improved seismic monitoring, earthquake modeling and ground motion simulation for early warning and hazard estimates in north Iceland. In S. Jónsson, B. Halldórsson, K. Jónsdóttir, P. Einarsson, R. Stefánsson, H. E. Ingólfsdóttir, et al. (Eds.), *Proceedings of the northquake 2019 workshop*, Husavik, North Iceland, 21–24 May 2019 (pp. 124–127). Retrieved from https://hac.is/wp-content/uploads/Northquake2019.pdf
Halldorsson, B., & Papageorgiou, A. S. (2012). Variations of the specific barrier model—Part II: Effect of isochron distributions. *Bulletin of Earthquake Engineering*, *10*(4), 1321–1337. https://doi.org/10.1007/s10518-012-9345-z
Harris, R. A., Barall, M., Aagaard, B., Ma, S., Roten, D., Olsen, K., et al. (2018). A suite of exercises for verifying dynamic earthquake rupture codes. *Seismological Research Letters*, *89*(3), 1146–1162. https://doi.org/10.1785/0220170222
Hensch, M., & Guðmundsson, G., & the SIL Monitoring Group. (2013). Offshore seismicity with large azimuthal gaps: Challenges for the SIL network. In *Proceedings of the international workshop on earthquakes in North Iceland*, Húsavík, Iceland.
Hjartardóttir, Á., Einarsson, P., Magnúsdóttir, S., Björnsdóttir, Þ., & Brandsdóttir, B. (2016). Fracture systems of the Northern Volcanic Rift Zone, Iceland: An onshore part of the Mid-Atlantic plate boundary. *Geological Society, London, Special Publications*, *420*(1), 297–314. https://doi.org/10.1144/sp420.1
Hu, F., Zhang, Z., & Chen, X. (2016). Investigation of earthquake jump distance for strike-slip step overs based on 3-D dynamic rupture simulations in an elastic half-space. *Journal of Geophysical Research: Solid Earth*, *121*(2), 994–1006. https://doi.org/10.1002/2015jb012696

21699356, 2023, 6, Downloaded from https://agupubs.onlinelibrary.wiley.com/doi/10.1029/2022JB025886 by Cochrane Germany, Wiley Online Library on [20/02/2024]. See the Terms and Conditions (https://onlinelibrary.wiley.com/terms-and-conditions) on Wiley Online Library for rules of use; OA articles are governed by the applicable Creative Commons License

Huang, Y., & Ampuero, J.-P. (2011). Pulse-like ruptures induced by low-velocity fault zones. *Journal of Geophysical Research*, *116*(B12), B12307. https://doi.org/10.1029/2011jb008684

Ida, Y. (1972). Cohesive force across the tip of a longitudinal-shear crack and Griffith's specific surface energy. *Journal of Geophysical Research*, *77*(20), 3796–3805. https://doi.org/10.1029/jb077i020p03796

Käser, M., Hermann, V., & Puente, J. D. L. (2008). Quantitative accuracy analysis of the discontinuous Galerkin method for seismic wave propagation. *Geophysical Journal International*, *173*(3), 990–999. https://doi.org/10.1111/j.1365-246x.2008.03781.x

Kowsari, M., Halldorsson, B., Jónsson, S., & Jónsson, S. (2021). Effects of different empirical ground motion models on seismic hazard maps for North Iceland. *Soil Dynamics and Earthquake Engineering*, *148*, 106513. https://doi.org/10.1016/j.soildyn.2020.106513

Kowsari, M., Sonnemann, T., Halldorsson, B., Hrafnkelsson, B., Snæbjörnsson, J. Þ., & Jonsson, S. (2020). Bayesian inference of empirical ground motion models to pseudo-spectral accelerations of south Iceland seismic zone earthquakes based on informative priors. *Soil Dynamics and Earthquake Engineering*, *132*, 106075. https://doi.org/10.1016/j.soildyn.2020.106075

Kyriakopoulos, C., Oglesby, D., Rockwell, T., Meltzner, A., Barall, M., Fletcher, J. M., & Tulanowski, D. (2019). Dynamic rupture scenarios in the Brawley seismic zone, Salton Trough, Southern California. *Journal of Geophysical Research: Solid Earth*, *124*(4), 3680–3707. https://doi.org/10.1029/2018jb016795

Liang, C., Ampuero, J.-P., & Pino Muñoz, D. (2022). The paucity of supershear earthquakes on large faults governed by rate and state friction. *Geophysical Research Letters*, *49*(22), e2022GL099749. https://doi.org/10.1029/2022gl099749

Liu, D., Duan, B., Prush, V. B., Oskin, M. E., & Liu-Zeng, J. (2021). Observation-constrained multicycle dynamic models of the Pingding Shan earthquake gate along the Altyn Tagh Fault. *Tectonophysics*, *814*, 228948. https://doi.org/10.1016/j.tecto.2021.228948

Liu, D., Duan, B., Scharer, K., & Yule, D. (2022). Observation-constrained multicycle dynamic models of the southern San Andreas and the northern San Jacinto faults: Addressing complexity in paleoearthquake extent and recurrence with realistic 2D fault geometry. *Journal of Geophysical Research: Solid Earth*, *127*(2), e2021JB023420. https://doi.org/10.1029/2021jb023420

Lozos, J. C. (2016). A case for historic joint rupture of the San Andreas and San Jacinto faults. *Science Advances*, *2*(3), e1500621. https://doi.org/10.1126/sciadv.1500621

Ma, S., Archuleta, R. J., & Page, M. T. (2007). Effects of large-scale surface topography on ground motions, as demonstrated by a study of the San Gabriel Mountains, Los Angeles, California effects of large-scale surface topography on ground motions. *Bulletin of the Seismological Society of America*, *97*(6), 2066–2079. https://doi.org/10.1785/0120070040

Magnúsdóttir, S., Brandsdóttir, B., Driscoll, N., & Detrick, R. (2015). Postglacial tectonic activity within the Skjálfandadjúp Basin, Tjörnes Fracture Zone, offshore Northern Iceland, based on high resolution seismic stratigraphy. *Marine Geology*, *367*, 159–170. https://doi.org/10.1016/j.margeo.2015.06.004

Mai, P., & Beroza, G. (2000). Source scaling properties from finite-fault-rupture models. *Bulletin of the Seismological Society of America*, *90*(3), 604–615. https://doi.org/10.1785/0119990126

Mai, P. M., Schorlemmer, D., Page, M., Ampuero, J.-P., Asano, K., Causse, M., et al. (2016). The earthquake-source inversion validation (SIV) project. *Seismological Research Letters*, *87*(3), 690–708. https://doi.org/10.1785/0220150231

Mai, P. M., Spudich, P., & Boatwright, J. (2005). Hypocenter locations in finite-source rupture models. *Bulletin of the Seismological Society of America*, *95*(3), 965–980. https://doi.org/10.1785/0120040111

Metzger, S., & Jónsson, S. (2014). Plate boundary deformation in North Iceland during 1992–2009 revealed by InSAR time-series analysis and GPS. *Tectonophysics*, *634*, 127–138. https://doi.org/10.1016/j.tecto.2014.07.027

Metzger, S., Jónsson, S., & Geirsson, H. (2011). Locking depth and slip-rate of the Húsavík Flatey fault, North Iceland, derived from continuous GPS data 2006–2010. *Geophysical Journal International*, *187*(2), 564–576. https://doi.org/10.1111/j.1365-246x.2011.05176.x

Nekrasova, A., Kossobokov, V., Peresan, A., & Magrin, A. (2014). The comparison of the NDSHA, PSHA seismic hazard maps and real seismicity for the Italian territory. *Natural Hazards*, *70*(1), 629–641. https://doi.org/10.1007/s11069-013-0832-6

Oeser, J., Bunge, H.-P., & Mohr, M. (2006). Cluster design in the Earth sciences tethys. In *International conference on high performance computing and communications* (pp. 31–40).

Oglesby, D. D. (2005). The dynamics of strike-slip step-overs with linking dip-slip faults. *Bulletin of the Seismological Society of America*, *95*(5), 1604–1622. https://doi.org/10.1785/0120050058

Oglesby, D. D. (2020). What can surface-slip distributions tell us about fault connectivity at depth? *Bulletin of the Seismological Society of America*, *110*(3), 1025–1036. https://doi.org/10.1785/0120190245

Oglesby, D. D., & Mai, P. M. (2012). Fault geometry, rupture dynamics and ground motion from potential earthquakes on the North Anatolian Fault under the Sea of Marmara. *Geophysical Journal International*, *188*(3), 1071–1087. https://doi.org/10.1111/j.1365-246x.2011.05289.x

Olsen, K., Day, S., Dalguer, L., Mayhew, J., Cui, Y., Zhu, J., et al. (2009). ShakeOut-D: Ground motion estimates using an ensemble of large earthquakes on the southern San Andreas fault with spontaneous rupture propagation. *Geophysical Research Letters*, *36*(4), L04303. https://doi.org/10.1029/2008gl036832

Oral, E., & Satriano, C. (2021). Future magnitude 7.5 earthquake offshore Martinique: Spotlight on the main source features controlling ground motion prediction. *Geophysical Journal International*, *227*(2), 1076–1093. https://doi.org/10.1093/gji/ggab245

Panzera, F., Zechar, J. D., Vogfjörd, K. S., & Eberhard, D. A. (2016). A revised earthquake catalogue for South Iceland. *Pure and Applied Geophysics*, *173*(1), 97–116. https://doi.org/10.1007/s00024-015-1115-9

Passarelli, L., Rivalta, E., Jónsson, S., Hensch, M., Metzger, S., Jakobsdóttir, S. S., et al. (2018). Scaling and spatial complementarity of tectonic earthquake swarms. *Earth and Planetary Science Letters*, *482*, 62–70. https://doi.org/10.1016/j.epsl.2017.10.052

Poliakov, A. N., Dmowska, R., & Rice, J. R. (2002). Dynamic shear rupture interactions with fault bends and off-axis secondary faulting. *Journal of Geophysical Research*, *107*(B11), ESE–6. https://doi.org/10.1029/2001jb000572

Power, W. L., & Tullis, T. E. (1991). Euclidean and fractal models for the description of rock surface roughness. *Journal of Geophysical Research*, *96*(B1), 415–424. https://doi.org/10.1029/90jb02107

Rodgers, A. J., Pitarka, A., Pankajakshan, R., Sjögreen, B., & Petersson, N. A. (2020). Regional-scale 3D ground-motion simulations of Mw 7 earthquakes on the Hayward fault, northern California resolving frequencies 0–10 Hz and including site-response corrections. *Bulletin of the Seismological Society of America*, *110*(6), 2862–2881. https://doi.org/10.1785/0120200147

Rögnvaldsson, S. T., Gudmundsson, A., & Slunga, R. (1998). Seismotectonic analysis of the Tjörnes Fracture Zone, an active transform fault in north Iceland. *Journal of Geophysical Research*, *103*(B12), 30117–30129. https://doi.org/10.1029/98jb02789

Roten, D., Olsen, K., Day, S., Cui, Y., & Fäh, D. (2014). Expected seismic shaking in Los Angeles reduced by San Andreas fault zone plasticity. *Geophysical Research Letters*, *41*(8), 2769–2777. https://doi.org/10.1002/2014gl059411

Roten, D., Olsen, K., & Pechmann, J. (2012). 3D simulations of M 7 earthquakes on the wasatch fault, Utah, Part II: Broadband (0–10 Hz) ground motions and nonlinear soil behavior. *Bulletin of the Seismological Society of America*, *102*(5), 2008–2030. https://doi.org/10.1785/0120110286

21699356, 2023, 6, Downloaded from https://agupubs.onlinelibrary.wiley.com/doi/10.1029/2022JB025886 by Cochrane Germany, Wiley Online Library on [20/02/2024]. See the Terms and Conditions (https://onlinelibrary.wiley.com/terms-and-conditions) on Wiley Online Library for rules of use; OA articles are governed by the applicable Creative Commons License

Ryan, K. J., & Oglesby, D. D. (2014). Dynamically modeling fault step overs using various friction laws. *Journal of Geophysical Research: Solid Earth*, *119*(7), 5814–5829. https://doi.org/10.1002/2014jb011151

Ryan, W. B., Carbotte, S. M., Coplan, J. O., O'Hara, S., Melkonian, A., Arko, R., et al. (2009). Global multi-resolution topography synthesis. *Geochemistry, Geophysics, Geosystems*, *10*(3). https://doi.org/10.1029/2008gc002332

Sagy, A., Brodsky, E. E., & Axen, G. J. (2007). Evolution of fault-surface roughness with slip. *Geology*, *35*(3), 283–286. https://doi.org/10.1130/g23235a.1

Savran, W., & Olsen, K. (2020). Kinematic rupture generator based on 3-D spontaneous rupture simulations along geometrically rough faults. *Journal of Geophysical Research: Solid Earth*, *125*(10), e2020JB019464. https://doi.org/10.1029/2020jb019464

Schmedes, J., Archuleta, R. J., & Lavallée, D. (2010). Correlation of earthquake source parameters inferred from dynamic rupture simulations. *Journal of Geophysical Research*, *115*(B3), B03304. https://doi.org/10.1029/2009jb006689

Scholz, C., Dawers, N., Yu, J.-Z., Anders, M., & Cowie, P. (1993). Fault growth and fault scaling laws: Preliminary results. *Journal of Geophysical Research*, *98*(B12), 21951–21961. https://doi.org/10.1029/93jb01008

Shi, Z., & Day, S. M. (2013). Rupture dynamics and ground motion from 3-D rough-fault simulations. *Journal of Geophysical Research: Solid Earth*, *118*(3), 1122–1141. https://doi.org/10.1002/jgrb.50094

Silva, V., Amo-Oduro, D., Calderon, A., Costa, C., Dabbeek, J., Despotaki, V., et al. (2020). Development of a global seismic risk model. *Earthquake Spectra*, *36*(1_suppl), 372–394. https://doi.org/10.1177/8755293019899953

Smith-Konter, B., & Sandwell, D. (2009). Stress evolution of the San Andreas fault system: Recurrence interval versus locking depth. *Geophysical Research Letters*, *36*(13), L13304. https://doi.org/10.1029/2009gl037235

Snaebjornsson, J., & Sigbjornsson, R. (2007). Earthquake action in Geothermal projects in NE Iceland at Krafla, Bjarnarflag, Gjastykki and Theistareykir: Assessment of geohazards affecting energy production and transmission systems emphasizing structural design criteria and mitigation of risk. Theistareykir Ltd, Landsnet, Landsvirkjun. (Tech. Rep.), Report no. LV-2007/075.

Socquet, A., Hollingsworth, J., Pathier, E., & Bouchon, M. (2019). Evidence of supershear during the 2018 magnitude 7.5 Palu earthquake from space geodesy. *Nature Geoscience*, *12*(3), 192–199. https://doi.org/10.1038/s41561-018-0296-0

Solnes, J., Sigbjörnsson, R., & Eliasson, J. (2004). Probabilistic seismic hazard mapping of Iceland. In *Proceedings of the 13th world conference on earthquake engineering*, Vancouver, BC, Canada.

Spudich, P., & Chiou, B. S. (2008). Directivity in NGA earthquake ground motions: Analysis using isochrone theory. *Earthquake Spectra*, *24*(1), 279–298. https://doi.org/10.1193/1.2928225

Spudich, P., Chiou, B. S., Graves, R., Collins, N., & Somerville, P. (2004). A formulation of directivity for earthquake sources using isochrone theory. U.S. Geological Survey Open-File Report, 1268 (54 pp.).

Spudich, P., Rowshandel, B., Shahi, S. K., Baker, J. W., & Chiou, B. S.-J. (2014). Comparison of NGA-West2 directivity models. *Earthquake Spectra*, *30*(3), 1199–1221. https://doi.org/10.1193/080313eqs222m

Stefansson, R., Gudmundsson, G. B., & Halldorsson, P. (2008). Tjörnes fracture zone. New and old seismic evidences for the link between the North Iceland rift zone and the Mid-Atlantic ridge. *Tectonophysics*, *447*(1–4), 117–126. https://doi.org/10.1016/j.tecto.2006.09.019

Strasser, F. O., Abrahamson, N. A., & Bommer, J. J. (2009). Sigma: Issues, insights, and challenges. *Seismological Research Letters*, *80*(1), 40–56. https://doi.org/10.1785/gssrl.80.1.40

Taufiqurrahman, T., Gabriel, A.-A., Ulrich, T., Valentova, L., & Gallovič, F. (2022). Broadband dynamic rupture modeling with fractal fault roughness, frictional heterogeneity, viscoelasticity and topography: The 2016 M_W 6.2 Amatrice, Italy earthquake. *Geophysical Research Letters*, *49*(22), e2022GL098872. https://doi.org/10.1029/2022gl098872

Thorgeirsson, Ó. (2011). *Historical earthquakes in North Iceland* (54 pp.). Húsavík Academic Centre.

Tinti, E., Casarotti, E., Ulrich, T., Taufiqurrahman, T., Li, D., & Gabriel, A.-A. (2021). Constraining families of dynamic models using geological, geodetic and strong ground motion data: The Mw 6.5, October 30th, 2016, Norcia earthquake, Italy. *Earth and Planetary Science Letters*, *576*, 117237. https://doi.org/10.1016/j.epsl.2021.117237

Ulrich, T., Gabriel, A.-A., Ampuero, J.-P., & Xu, W. (2019). Dynamic viability of the 2016 Mw 7.8 Kaikōura earthquake cascade on weak crustal faults. *Nature Communications*, *10*(1), 1–16. https://doi.org/10.1038/s41467-019-09125-w

Ulrich, T., Gabriel, A.-A., & Madden, E. H. (2022). Stress, rigidity and sediment strength control megathrust earthquake and tsunami dynamics. *Nature Geoscience*, *15*(1), 67–73. https://doi.org/10.1038/s41561-021-00863-5

Ulrich, T., Vater, S., Madden, E. H., Behrens, J., Dinther, Y. V., Zelst, I. V., et al. (2019). Coupled, physics-based modeling reveals earthquake displacements are critical to the 2018 Palu, Sulawesi Tsunami. *Pure and Applied Geophysics*, *176*(10), 4069–4109. https://doi.org/10.1007/s00024-019-02290-5

Wang, Y., & Day, S. M. (2020). Effects of off-fault inelasticity on near-fault directivity pulses. *Journal of Geophysical Research: Solid Earth*, *125*(7), e2019JB019074. https://doi.org/10.1029/2019jb019074

Wesnousky, S. G. (1988). Seismological and structural evolution of strike-slip faults. *Nature*, *335*(6188), 340–343. https://doi.org/10.1038/335340a0

Withers, K. B., Olsen, K. B., Day, S. M., & Shi, Z. (2019). Ground motion and intraevent variability from 3D deterministic broadband (0–7.5 Hz) simulations along a nonplanar strike-slip fault. *Bulletin of the Seismological Society of America*, *109*(1), 229–250. https://doi.org/10.1785/0120180006

Wollherr, S., Gabriel, A.-A., & Mai, P. M. (2019). Landers 1992 "reloaded": Integrative dynamic earthquake rupture modeling. *Journal of Geophysical Research: Solid Earth*, *124*(7), 6666–6702. https://doi.org/10.1029/2018jb016355

Wollherr, S., Gabriel, A.-A., & Uphoff, C. (2018). Off-fault plasticity in three-dimensional dynamic rupture simulations using a modal Discontinuous Galerkin method on unstructured meshes: Implementation, verification and application. *Geophysical Journal International*, *214*(3), 1556–1584. https://doi.org/10.1093/gji/ggy213

Ziegler, M., Rajabi, M., Heidbach, O., Hersir, G. P., Ágústsson, K., Árnadóttir, S., & Zang, A. (2016). The stress pattern of Iceland. *Tectonophysics*, *674*, 101–113. https://doi.org/10.1016/j.tecto.2016.02.008

21699356, 2023, 6, Downloaded from https://agupubs.onlinelibrary.wiley.com/doi/10.1029/2022JB025886 by Cochrane Germany, Wiley Online Library on [20/02/2024]. See the Terms and Conditions (https://onlinelibrary.wiley.com/terms-and-conditions) on Wiley Online Library for rules of use; OA articles are governed by the applicable Creative Commons License